

Alma Mater Studiorum Università di Bologna
Archivio istituzionale della ricerca

A Catalog of Emission-line Galaxies from the Faint Infrared Grism Survey: Studying Environmental Influence on Star Formation

This is the final peer-reviewed author's accepted manuscript (postprint) of the following publication:

Published Version:

Pharo J., Malhotra S., Rhoads J.E., Pirzkal N., Finkelstein S.L., Ryan R., et al. (2020). A Catalog of Emission-line Galaxies from the Faint Infrared Grism Survey: Studying Environmental Influence on Star Formation. THE ASTROPHYSICAL JOURNAL, 888(2), 1-19 [10.3847/1538-4357/ab5f5c].

Availability:

This version is available at: <https://hdl.handle.net/11585/802988> since: 2021-02-22

Published:

DOI: <http://doi.org/10.3847/1538-4357/ab5f5c>

Terms of use:

Some rights reserved. The terms and conditions for the reuse of this version of the manuscript are specified in the publishing policy. For all terms of use and more information see the publisher's website.

This item was downloaded from IRIS Università di Bologna (<https://cris.unibo.it/>).
When citing, please refer to the published version.

(Article begins on next page)

This is the final peer-reviewed accepted manuscript of:

John Pharo, Sangeeta Malhotra, James E. Rhoads, Norbert Pirzkal, Steven L. Finkelstein, Russell Ryan, Andrea Cimatti, Lise Christensen, Nimish Hathi, Anton Koekemoer, Santosh Harish, Mark Smith, Amber Straughn, Rogier Windhorst, Ignacio Ferreras, Caryl Gronwall, Pascale Hibon, Rebecca Larson, Robert O'Connell, Anna Pasquali, and Vithal Tilvi, A Catalog of Emission-line Galaxies from the Faint Infrared Grism Survey: Studying Environmental Influence on Star Formation, The Astrophysical Journal, 2020, Volume 888, Number 2 , Article 79.

The final published version is available online at: <http://dx.doi.org/10.3847/1538-4357/ab5f5c>

Rights / License:

The terms and conditions for the reuse of this version of the manuscript are specified in the publishing policy. For all terms of use and more information see the publisher's website.

This item was downloaded from IRIS Università di Bologna (<https://cris.unibo.it/>)

When citing, please refer to the published version.

A Catalog of Emission-Line Galaxies from the Faint Infrared Grism Survey: Studying Environmental Influence on Star Formation

JOHN PHARO,¹ SANGEETA MALHOTRA,^{2,1} JAMES E. RHOADS,^{2,1} NORBERT PIRZKAL,³
STEVEN L. FINKELSTEIN,⁴ RUSSELL RYAN,³ ANDREA CIMATTI,^{5,6} LISE CHRISTENSEN,⁷
NIMISH HATHI,³ ANTON KOEKEMOER,³ SANTOSH HARISH,¹ MARK SMITH,¹ AMBER STRAUGHN,²
ROGIER WINDHORST,¹ IGNACIO FERRERAS,⁸ CARYL GRONWALL,^{9,10} PASCALE HIBON,¹¹
REBECCA LARSON,⁴ ROBERT O'CONNELL,¹² ANNA PASQUALI,¹³ AND VITHAL TILVI¹

¹*School of Earth and Space Exploration, Arizona State University, Tempe, AZ 85287, USA*

²*NASA's Goddard Space Flight Center, Astrophysics Science Division, Code 660, Greenbelt, MD 20771 USA*

³*Space Telescope Science Institute, Baltimore, MD 21218, USA*

⁴*Department of Astronomy, The University of Texas at Austin, Austin, TX 78712, USA*

⁵*Department of Physics and Astronomy (DIFA), University of Bologna, Via Gobetti 93/2, I-40129, Bologna, Italy*

⁶*INAF Osservatorio Astrofisico di Arcetri, Largo E. Fermi 5, I-50125, Firenze, Italy*

⁷*1 Dark Cosmology Centre, Niels Bohr Institute, University of Copenhagen, Juliane Maries Vej 30, DK-2100 Copenhagen, Denmark*

⁸*Mullard Space Science Laboratory, University College London, Holmbury St. Mary, Dorking, Surrey RH5 6NT, UK*

⁹*Department of Astronomy & Astrophysics, Pennsylvania State University, University Park, PA 16802*

¹⁰*Institute for Gravitation & the Cosmos, Pennsylvania State University, University Park, PA 16802*

¹¹*ESO, Alonso de Cordova 3107, Santiago, Chile*

¹²*The University of Virginia, Charlottesville, VA 22904-4325, USA*

¹³*Astronomisches Rechen-Institut, Zentrum fuer Astronomie, Universitaet Heidelberg, Moenchhofstrasse 12-14, D-69120 Heidelberg, Germany*

ABSTRACT

We present a catalog of 208 $0.3 < z < 2.1$ Emission Line Galaxies (ELG) selected from 1D slitless spectroscopy obtained using Hubble's WFC3 G102 grism, as part of the Faint Infrared Grism Survey (FIGS). We identify ELG candidates by searching for significant peaks in all continuum-subtracted G102 spectra, and, where possible, confirm candidates by identifying consistent emission lines in other available spectra or with published spectroscopic redshifts. We provide derived emission line fluxes and errors, redshifts, and equivalent widths (EW) for $H\alpha$ $\lambda 6563$, $[OIII]\lambda\lambda 4959, 5007$, and $[OII]\lambda\lambda 3727$ emission lines, for emission line galaxies down to $AB(F105W) > 28$ and $> 10^{-17}$ erg cm⁻² s⁻¹ line flux. We use the resulting line catalog to investigate a possible relationship between line emission and a galaxy's environment. We use 7th-nearest-neighbor distances to investigate the typical surroundings of ELGs compared to non-ELGs, and we find that $[OIII]$ emitters are preferentially found at intermediate galaxy densities near galaxy groups. We characterize these ELGs in terms of the galaxy specific star formation rate (SSFR) versus stellar mass, and find no significant influence

of environment on that relation. We calculate star formation rates (SFR), and find no dependence of SFR on local galaxy surface density for $0.3 < z < 0.8$ H α emitters and for $0.8 < z < 1.3$ [OIII] emitters. We find similar rates of close-pair interaction between ELGs and non-ELGs. For galaxy surface densities $\Sigma \leq 30 \text{ Mpc}^{-2}$, we find no consistent effect of environment on star formation.

Keywords: galaxies

1. INTRODUCTION

The detection and measurement of nebular line emission in galaxies has long been a useful tool in the study of galaxy evolution. Hydrogen recombination lines, such as H α $\lambda 6563$ and H β $\lambda 4861$, and forbidden transitions in ionized oxygen, such as [OIII] $\lambda\lambda 4959, 5007$ and [OII] $\lambda 3727$, can be used to measure a galaxy’s recent star formation (Kennicutt 1998), its gas-phase composition (Kobulnicky and Zaritsky 1999), and dust extinction (Calzetti et al. 1994), among other properties. Furthermore, the spectroscopic identification of an emission line enables the measurement of a galaxy’s redshift with much higher precision than is achievable with methods relying on broadband photometry alone, even with relatively low-resolution slitless spectroscopy or narrowband photometry (Xu et al. 2007; Xia et al. 2011; Ferreras et al. 2014; Pharo et al. 2018). Measurements of fundamental galaxy properties like luminosity, as well as assessments of a galaxy’s interactions with nearby galaxies and their environments, rely in part on this measure of distance.

A key aspect of the study of galaxy evolution is the potential influence of a galaxy’s surrounding environment on its development, particularly in how it relates to star formation. In the local universe, red, passive galaxies are associated with overdensities, while blue galaxies with active star formation (of which line emission is an indicator) are more likely found in low-density environments and lower-mass dark matter halos (Dressler 1980; Balogh et al. 2004; Kauffmann et al. 2004) and in galaxies with lower stellar mass (Pasquali et al. 2009). At higher redshift, the picture is less clear, with some studies matching the local result (Patel et al. 2009), while others find a weak star formation dependence on environment (Grützbauch et al. 2011a; Scoville et al. 2013). Elbaz et al. (2007) and Cooper et al. (2008) find that star formation activity correlates with density at high redshift, and Tran et al. (2010) find a high level of star formation in a cluster core at $z = 1.62$ compared to lower densities, the opposite of the local trend. Sobral et al. (2011) and Darvish et al. (2014) report an increase in star formation at intermediate density, potentially associated with groups or filaments rather than rich clusters. In order to make clearer sense of this picture, further studies capable of accurately measuring both local environments and star formation are needed. The identification of line emission in galaxies can achieve this purpose.

Emission line galaxies (ELGs) can be detected in several ways. In principle, the most straightforward method is the use of ground-based spectroscopy, but this is not always practical for the faintest objects, requiring some pre-selection of targets and spectral features. Another common approach is the use of narrowband photometric surveys (e.g., Boroson et al. 1993; Rhoads et al. 2001; Geach et al. 2008; Sobral et al. 2011, 2012; Coughlin et al. 2018), which detect emission lines by measuring the flux excess between narrowband photometry and nearby broadband photometry. This method is useful for obtaining a large number of detections, but these detections are limited to a narrow redshift window defined by the width of the narrowband.

A third approach for ELG detection is the use of low-resolution, slitless spectroscopy. Recent surveys have made use of the Hubble Space Telescope’s (HST) ACS (APPLES, [Pasquali et al., 2003](#); GRAPES, [Pirzkal et al.](#); [Malhotra et al.](#); [Rhoads et al., 2004](#); PEARS, [Pirzkal et al.](#); [Rhoads et al., 2009](#)), Wide-Field Camera 3 (WFC3) G102 (WISP, [Atek et al., 2010](#); GLASS, [Treu et al., 2015](#); FIGS, [Pirzkal et al., 2018](#)), and G141 (WISP, [Atek et al., 2010](#); GLASS, [Treu et al., 2015](#); 3D-HST, [Momcheva et al., 2016](#)) grisms to identify ELGs over a broad redshift range ($0 < z < 7.5$) and without a pre-selection of targets that might exclude continuum-faint sources ([Rhoads et al. 2013](#); [Tilvi et al. 2016](#); [Larson et al. 2018](#)). In the Faint Infrared Grism Survey (FIGS; [Pirzkal et al. 2017](#)), we apply this approach with deep WFC3 G102 observations taken at multiple position angles in order to maximize emission line sensitivity, minimize spectral contamination, and more accurately measure the central wavelengths of emission lines ([Xu et al. 2007](#); [Straughn et al. 2008, 2009](#); [Xia et al. 2011, 2012](#); [Pirzkal et al. 2013](#)).

The FIGS grism data therefore provides an opportunity to study how an ELG’s emission properties relate to its environment. First, the slitless grism selection enables the unbiased detection of continuum-faint ELGs, which can be used for a study of star formation in the FIGS fields. Second, grism studies have shown that the combination of grism spectroscopy with broadband photometry can significantly improve photometric redshift accuracy ([Ryan et al. 2007](#); [Brammer et al. 2012](#); [Pharo et al. 2018](#)), and that these improved redshift catalogs can be used to better identify and study galaxy overdensities ([Pharo et al. 2018](#)). With FIGS data, we can then measure emission lines and star formation rates (SFRs) across a broad redshift range, and evaluate their local environments using improved grism redshifts.

In this paper, we present a catalog of emission line galaxies derived from an automated search of 1D slitless spectra from FIGS obtained with HST’s WFC3 G102 grism. In this catalog, we list the line fluxes, redshifts, and observed equivalent widths (EW) for 208 strong-line ($H\alpha$, $[OIII]\lambda\lambda 5007, 4959$, and $[OII]\lambda 3727$) emitters in a redshift range of $0.3 < z < 2.1$. We then combine this catalog with a previous study of overdensities in the FIGS fields ([Pharo et al. 2018](#)) to study ELG properties as a function of their local galaxy environment. In §2, we briefly describe the FIGS data collection and reduction, as well as the sources of additional spectra we used to supplement our study. In §3, we detail our search methods for identifying and confirming ELG candidates in 1D spectra. In §4, we describe our line flux measurements, present the final ELG catalog, and summarize its properties. In §5, we study these properties as functions of the local environment and stellar mass. For this paper we will use $H_0 = 67.3 \text{ km s}^{-1} \text{ Mpc}^{-1}$ and $\Omega_M = 0.315$, $\Omega_\Lambda = 0.685$ ([Planck Collaboration et al. 2015](#)). All magnitudes are given in the AB system ([Oke and Gunn 1983](#)).

2. SURVEY DESCRIPTION AND DATA

2.1. FIGS Observations

The Faint Infrared Grism Survey (FIGS, HST Cycle 22, PID:13779, PI S. Malhotra) used the HST WFC3-G102 infrared grism (see Figure 1) to obtain deep slitless spectroscopy of ~ 6000 galaxies. FIGS achieved 40-orbit depth in 4 fields within the greater GOODS-North and GOODS-South fields ([Giavalisco et al. 2004](#)), designated GN1, GN2, GS1 (HUDF), and GS2 (HDF-PAR2). Objects in each field were observed in 5 different 8-orbit position angles (PAs) in order to mitigate the contamination of spectra from overlapping spectra from nearby objects. The grism image at each

PA covers a $2.05' \times 2.27'$ field of view, and the G102 grism has a resolution of 24.5 \AA per pixel. The total area of coverage over all fields is 17.7 square arcminutes.

2.2. Spectral Extraction and Properties

In this paper, we used 1D spectra of individual PAs which were generated using the methods described in Pirzkal et al. (2017). Here we briefly summarize this process. We reduced FIGS data in a manner that loosely follows the method used for GRAPES and PEARS, the previous deep HST grism surveys (Pirzkal et al. 2004; Malhotra et al. 2005; Xu et al. 2007; Rhoads et al. 2009; Straughn et al. 2009; Xia et al. 2012; Pirzkal et al. 2013). First, we generated a master catalog of sources from deep CANDELS survey mosaics in the F850LP filter in ACS and the F125W and F160W filters in WFC3 (approximately the z, J, and H bands; Grogin et al. 2011; Koekemoer et al. 2011). We astrometrically corrected the data to match the absolute astrometry of the GOODS V2.0 catalogs. We estimated the background levels of the grism observations by using a two-component model, which included a constant Zodiacal light background, as well as a varying He I light background. To generate the individual spectra, we used a Simulation Based Extraction (SBE) approach that accounts for spectral contamination from overlapping spectra, as well as allowing the use of an optimal extraction approach (Horne 1986) when generating 1D spectra from 2D spectra. We refer the reader to Pirzkal et al. (2017) for a complete description of these processes. Pirzkal et al. (2017) also describes a method for combining individual PAs into a single 1D spectrum, though we do not use the combined spectra here. Individual PAs are subject to different levels of contamination, and depending on the location of the emission line region, they may not all exhibit the same line emission. For these reasons, we use the individual PA spectra for our ELG search and analysis.

We initially extracted all sources down to a continuum level of $F_{105W} < 30$ mag. When the extractions were complete, we had an average of ~ 1700 spectra per field, with a typical 3σ continuum detection limit of $m_{F105W} = 26$ mag and an emission line sensitivity of $10^{-17} \text{ erg cm}^{-2} \text{ s}^{-1}$. The middle panel of Figure 1 shows the throughput curve for the G102 grism compared to other spectral and broadband curves. We restricted use of the G102 spectra to wavelengths between 8500 and 11500 \AA , where the grism throughput is greater than 20%.

2.3. Additional Spectral Data

2.3.1. MUSE/VLT

For the GS1/HUDF FIGS field, we supplemented our infrared FIGS spectra with deep archival high-resolution optical IFU spectra taken with the Multi-Unit Spectroscopic Explorer (MUSE) instrument (Bacon et al. 2010) from the Very Large Telescope (VLT). This expands the available spectroscopic wavelength coverage for the GS1 field considerably, enabling confirmation of detected emission lines in FIGS via the identification of complementary emission lines at optical wavelengths, even for many faint sources. We used the publicly available IFU spectra from the MUSE Hubble Ultra Deep Survey (Bacon et al. 2017), a mosaic of nine $1 \times 1 \text{ arcmin}^2$ MUSE fields in the HUDF. The data were reduced using standard procedures and ESO pipelines. After the initial reduction steps of each observations, offsets between pointings in the mosaic were found by cross correlations and matching stars at the areas of overlapping mosaics. The 180 cubes were then combined with ESOREX again. This product was cleaned of strong sky subtraction residuals using ZAP (Zurich Atmosphere Purging) by Soto et al. (2016).

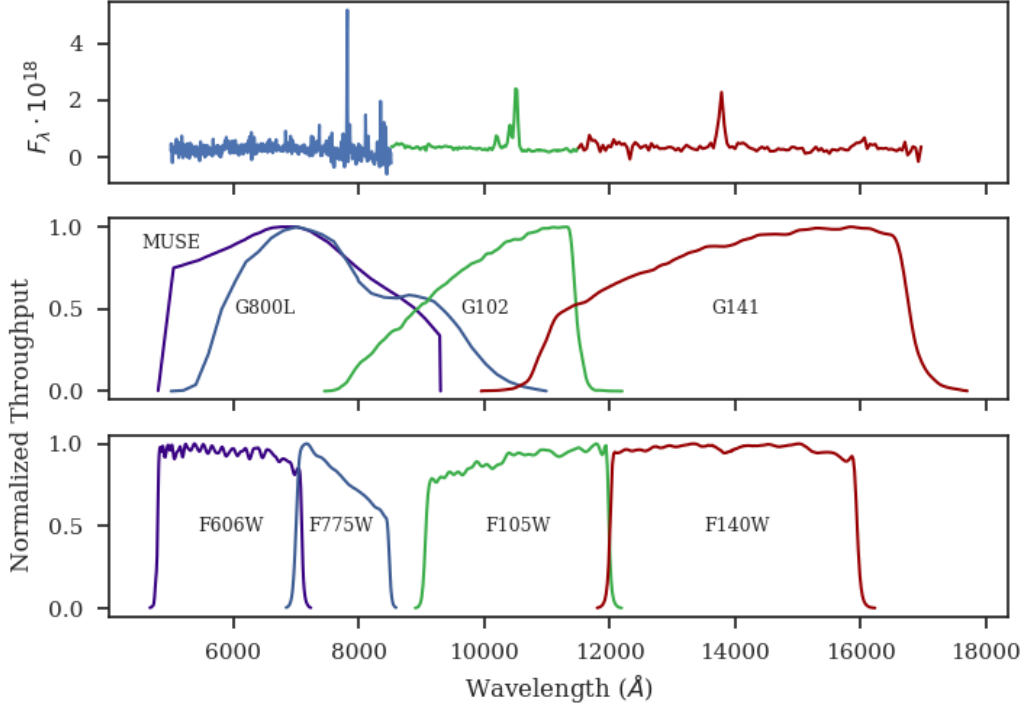


Figure 1. The top panel shows the spectrum of an example ELG from FIGS at $z=1.098$, with spectra from MUSE/VLT (dark blue), the HST ACS G800L grism (blue), the HST WFC3 G102 grism (green), and the G141 grism (red). The y-axis for this panel is in units of 10^{-18} ergs $\text{s}^{-1} \text{cm}^{-2} \text{\AA}^{-1}$. The middle panel gives the throughput curves for each spectrograph, normalized to the maximum throughput of each. The lower panel shows the throughput curves for HST photometric bands at comparable wavelengths. In this example, $[\text{OIII}]\lambda\lambda 4959, 5007$ are detected in the FIGS G102 spectrum, with $\text{H}\alpha + [\text{NII}]$ detected in G141, and $[\text{OII}]\lambda 3727$ detected in MUSE/VLT.

In order to extract spectra for emission-line objects in our sample, we first used the known sky coordinates for each object in FIGS to find RA-Dec matches in the MUSE datacube. At each wavelength slice, we placed a $2''$ aperture centered on the object, which we determined was able to capture the total flux from most line-emitting sources at the redshifts considered. Then, we generated 1D spectra for the matched objects by summing up the flux within the aperture at each wavelength, across the entire MUSE wavelength range (see Figure 1 for the MUSE wavelength coverage compared to WFC3 G102), using the MPDAF software package (Bacon et al. 2016). This produced a catalog of extracted FIGS candidate spectra from the reduced MUSE datacube. The MUSE data wavelength coverage extends from 4752 \AA to 9347 \AA with a spectral resolution of 2.3 \AA , though the sensitivity begins to drop off at wavelengths lower than 5000 \AA , and at wavelengths higher than 9200 \AA , the noise from sky emission begins to dominate, so we restrict our usage of the MUSE spectra to between these wavelengths. MUSE has a 3σ line sensitivity of $\sim 3 \cdot 10^{-19} \text{ erg cm}^{-2} \text{ s}^{-1}$, and thus should detect lines of strength comparable to or even considerably less than the lines found in FIGS G102 spectra.

2.3.2. *G800 Grism Data*

In the GS1/HUDF field, we were also able to make use of line identifications from the Grism ACS Program for Extragalactic Science (GRAPES) (Xu et al. 2007), which used the G800L grism from HST ACS, a low-resolution (40 Å per pixel at 8000 Å) optical grism. Xu et al. (2007) were able to identify lines from ~ 6000 Å to ~ 9500 Å, a similar region of coverage to VLT/MUSE. This enabled us to search for complementary optical lines for FIGS sources while simultaneously confirming some ELGs from GRAPES.

2.3.3. *G141 Grism Data*

In the other FIGS fields (GN1, GN2, GS2), we also made use of archival WFC3 G141 grism spectra (Ryan 2013, HST proposal ID 13266) collected from the WISP (Atek et al. 2010) and 3D-HST (Brammer et al. 2012; Momcheva et al. 2016) surveys. Inclusion of this data effectively extended the FIGS spectral coverage out to ~ 1.7 micron. These additional collected G141 spectra are not as deep as the FIGS G102 data, with $> 90\%$ completeness down to $J < 24$ mag. They also have lower spectral resolution than the WFC3 G102 spectra (46.5 Å per pixel at 14000 Å) and thus were of limited use for candidate confirmation, but they allowed for the detection of strong line emission in some objects.

2.3.4. *Spectroscopic Redshifts*

We assembled compilations of published high-quality spectroscopic redshifts (spec-zs) in the GOODS-N and CDFS fields (N. Hathi, private communication). These fields are well-studied, and the existence of independent spectroscopy allowed us to confirm the emission-line-derived redshifts (and thus, the identified emission line) of some of our brighter sources. Many of the published spec-z catalogs included quality designations distinguishing the reliability of different spectra. The exact scales of quality used differed somewhat between surveys, but we generally used only those results deemed “good” or better by the original survey. Our compilations included spec-zs from Wirth et al. (2004), Malhotra et al. (2005), Grazian et al. (2006), Pasquali et al. (2006), Reddy et al. (2006), Ravikumar et al. (2007), Barger et al. (2008), Hathi et al. (2008), Straughn et al. (2008), Vanzella et al. (2008), Wuyts et al. (2008), Ferreras et al. (2009), Hathi et al. (2009), Rhoads et al. (2009), Straughn et al. (2009), Vanzella et al. (2009), Wuyts et al. (2009), Balestra et al. (2010), Silverman et al. (2010), Yoshikawa et al. (2010), Cooper et al. (2011), Xue et al. (2011), Cooper et al. (2012), Ono et al. (2012), Finkelstein et al. (2013), Kurk et al. (2013), Le Fevre et al. (2013), Pirzkal et al. (2013), Trump et al. (2013), Song et al. (2014), Kriek et al. (2015), Le Fevre et al. (2015), Morris et al. (2015), Wirth et al. (2015), Trump et al. (2015), Momcheva et al. (2016), Herenz et al. (2017), Inami et al. (2017), and McLure et al. (2018).

3. EMISSION LINE IDENTIFICATION METHODS

3.1. *Search for ELG Candidates*

We conducted a blind search for ELGs among the FIGS 1D spectra. Because we obtained our infrared spectra via slitless grism spectroscopy, there was no pre-selection of ELG candidates before the search via the placement of slits or by broadband magnitude cutoffs beyond the survey depth. This had the advantage of enabling the detection of ELGs with potentially very low continuum levels, and so might allow for the identification and study of smaller and/or fainter galaxies with nebular

line emission. However, this did require an efficient method for selecting ELG candidates from the total sample of FIGS spectra. In order to search the ~ 6000 FIGS spectra for emission lines, we developed a code to automatically search for and identify significant peaks in a 1D spectrum.

First, the level of the continuum flux had to be estimated at each wavelength element in the 1D spectrum. To measure this, we used a median-flux filter, which assumes a prospective line width and calculates the local continuum from the median flux outside that line width, in wavelength regions on either side of the line. A given wavelength λ_0 is taken to be the center of a potential line. The potential line flux is measured as all the flux contained within a line width $2\Delta\lambda_1$, so that the algorithm defines the potential line as the region covered by:

$$\lambda_0 - \Delta\lambda_1 < \lambda < \lambda_0 + \Delta\lambda_1 \quad (1)$$

Then the code estimates the nearby continuum by looking at regions to either side of the line with width $\Delta\lambda_2$. The nearby continuum is defined then as the regions contained in:

$$(\lambda_0 - \Delta\lambda_1) - \Delta\lambda_2 < \lambda < (\lambda_0 - \Delta\lambda_1) \text{ and } (\lambda_0 + \Delta\lambda_1) < \lambda < (\lambda_0 + \Delta\lambda_1) + \Delta\lambda_2 \quad (2)$$

The algorithm then takes the median flux of the wavelength pixels constrained by Equation 2 as an estimate of the local continuum around the hypothetical line, and subtracts this flux from the flux at λ_0 in order to obtain the continuum-subtracted or residual flux at that point. If there is a line present at λ_0 , this method allows for measurement of the level of the continuum without influence from the line flux. The code takes the standard deviation among this set of continuum fluxes as an estimate of the flux error at λ_0 . If λ_0 is too near the edge of the spectrum to measure $\Delta\lambda_2$ on both sides, we estimate the continuum based on the fluxes from just the complete side. The algorithm repeats this process, iterating over each wavelength element in a given spectrum, estimating the continuum flux at that wavelength, and subtracting it. We refer to Figure 2 for an example continuum-subtracted spectrum. We were able to best minimize false detections while retaining real ones with $2\Delta\lambda_1 = 122.5 \text{ \AA}$ and $\Delta\lambda_2 = 147 \text{ \AA}$, based on tests of variable $\Delta\lambda_1$ and $\Delta\lambda_2$ with a preliminary subsample of ELGs with matching spectroscopic redshifts.

After the spectrum is continuum-subtracted, the code calculates the signal-to-noise ratio (S/N) at each wavelength with the residual flux and the flux error, once more iterating through the list of wavelength elements. The sum of the fluxes constrained by Equation 1 determines the hypothetical line signal, and the estimated flux errors added in quadrature measure the noise of the hypothetical line. After this calculation is complete for all wavelengths, the algorithm identifies the location with maximum line S/N in the spectrum. If $S/N > 5$, we fit a Gaussian at the central wavelength element from which we obtain a measure of the continuum-subtracted integrated line flux. The code then subtracts the fit line from the residual flux spectrum and checks the next-highest S/N . If the S/N ratio still exceeds 5, the routine repeats until the peak S/N ratio is below the detection threshold.

We run this routine on the individual PA spectra in each field, and record all instances of $S/N > 5$. If the code finds a peak in at least two PAs with centroids at the same or adjacent wavelength elements (24.5 \AA in either direction), it declares a detection. Lower S/N thresholds produced numerous false positives, so we used the $S/N > 5$ cutoff to maintain a more robust sample. We avoided using simultaneous fits of all PAs in order to avoid including contaminated PAs in a combined significance measurement. With individual PA fits, contaminated detections could more easily be identified and

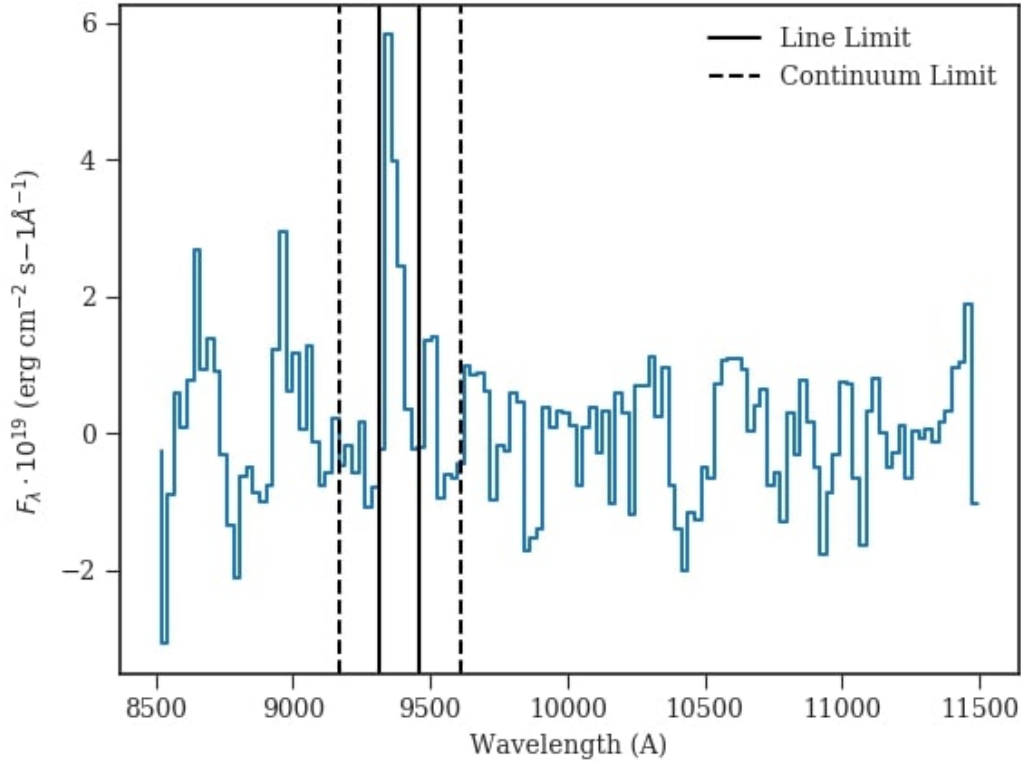


Figure 2. The continuum-subtracted 1D spectrum of one position angle of one FIGS ELG: ID GS1-2375. This figure shows a snapshot of the continuum-subtraction and line-finding routine. The routine identifies a “test line” region with a given pixel width, shown here as the region contained within the solid vertical lines. Next the routine uses the pixels between the solid lines and the dashed lines to estimate the local continuum flux, and subtracts that flux from the test line. Then the routine estimates the S/N ratio of the continuum-subtracted test line, and if the ratio surpasses the 5σ threshold, it reports a possible detection. This process iterates over each wavelength element in the spectrum.

removed. After running the routine over all galaxies in the field, the list of detections forms an ELG candidate list.

3.2. Line Identification and Confirmation

Once we had obtained lists of candidate detections for each field, we next attempted to identify the type of emission line detected in each spectrum. First, we matched the candidate lists to our photometric redshift (photo-z) catalog (Pharo et al. 2018) and assigned a preliminary line ID based on the likely redshift. For the purposes of this result, we focused on three strong line IDs that could be robustly detected at FIGS resolution and sensitivity: $H\alpha\lambda 6563$, $[\text{OIII}]\lambda\lambda 4959, 5007$, and $[\text{OII}]\lambda 3727$. We did this because these lines typically have the strongest emission, and therefore can be detected robustly, and because they are common features of star-forming galaxies. $H\beta 4861$ could theoretically be resolved and detected alongside $[\text{OIII}]$, but was typically faint enough that it was difficult to detect at a significant level. Other FIGS studies have looked at $\text{Ly}\alpha$ line emission at higher redshifts (Tilvi et al. 2016; Larson et al. 2018). We measure detections of GS2-1406 at levels of significance $\geq 3.5\sigma$,

consistent with those measured by [Larson et al. \(2018\)](#), though these are lower than the 5σ cut used in this work. We detect GN1-1292 significantly in only one of the two PAs where it is measured in [Tilvi et al. \(2016\)](#). [Pirzkal et al. \(2018\)](#) also detects GS2-1406 but not GN1-1292.

After the preliminary photo- z identification, we sought to confirm the existence and type of the line by checking the detection against ancillary data. The most straightforward way to do this was to check for other emission lines. Since the wavelength ratio between a given pair of emission lines is invariant across redshift, the detection of two strong lines is a useful check. For eight candidates, two strong lines were measured in the FIGS G102 spectra alone, and for 59 others we identified pairs by checking matched ACS/G800L, MUSE/VLT, and WFC/G141 spectra (described in §2.3). This most commonly involved finding $H\alpha$ -[OIII] and [OIII]-[OII] pairs. Occasionally, we were able to identify another spectral feature, such as a strong 4000 Å break, in order to confirm the redshift. We note that while finding a matching line can confirm a line detection, not finding a matching line does not necessarily mean the detection is false, since the true relative line strengths are not known ahead of time. The matching line may be sufficiently weaker than the FIGS line, or the matching spectra sufficiently shallow, such that the matching line is not detected.

If matching spectra were not available, or a strong line was not identified, we next checked for a matching spectroscopic redshift (spec- z). If a spec- z assigned the line peak-wavelength a restframe wavelength that matched an emission line within the wavelength range of a FIGS grism element, we assigned the line the spec- z ID. If neither matching lines nor spec- z IDs were available, then we let the photo- z identification stand.

In each field, there were a handful of objects with a significant detection but no good redshift measurement. These were almost all very continuum faint ($F105W > 27.5$ mag) objects, which both reduced the availability of broadband fluxes to use for photometric redshift fits and made the spectra more susceptible to contamination from nearby sources. Consequently, most of these candidates were removed through visual inspection, leaving four likely ELGs with no redshift: GS1-1062, GS2-532, GS2-838, and GS2-1624.

With the lines identified, we compared our results to the line list derived from [Pirzkal et al. \(2018\)](#), a study of FIGS strong line emitters using a distinct identification method with FIGS 2D spectra. In this paper, we do an independent selection and measurement of ELGs so as not to bias the findings of different search methods. However, we have compared our line candidates with those found in [Pirzkal et al. \(2018\)](#) and find them to be in close agreement, with a 90% match in identifications. A complete match would have been highly unlikely, as the methods have different strengths. The 2D method performs better at identifying broader lines that are wider than the median filter used with the 1D search. As described in §3.1, we experimented with different median filter widths when designing the 1D search, and found that expanding the filter too broadly tended to introduce false detections and make it more difficult to detect fainter objects, since the detection becomes more susceptible to changes in the continuum. The 2D method, however, requires detections in at least 3 PAs. For a given FIGS field, the different roll angles do not overlap completely, so near the edges of the field there are regions without the full 5 PA coverage. In these regions, it is easier to get a detection with the 1D method, as it requires detections in only 2 PAs.

Table 1. Median Properties of Emission Line Galaxies

Line	Number	z	Flux ($\text{erg cm}^{-2} \text{s}^{-1}$)	σ_F/F^a	F105W Mag	EW (\AA)
H α λ 6563	71	0.56	$8.1 \cdot 10^{-17}$	14%	22.9	42
[OIII] $\lambda\lambda$ 4959,5007	81	0.99	$5.3 \cdot 10^{-17}$	21%	24.3	67
[OII] λ 3727	56	1.76	$3.5 \cdot 10^{-17}$	20%	24.2	53

^aThe median flux error as a percentage of the median line flux.

4. FLUX CATALOG

With a robust ELG list, we next systematically fit the strong emission lines in order to obtain flux measurements and more precise line centers (and therefore redshifts). To do this, we used a combined Gaussian fit to the line and power-law fit to the local continuum, using a Python coding package called *lmfit* (Newville et al. 2014). The peak-finding routine (§3.1) provided first estimates for the wavelength of the line center and the flux level of the nearby continuum. We restricted the possible wavelength of the line center allowed by the fit to only vary by the width of one grism element in either direction from this initial guess.

For the H α line, the nearby [NII] $\lambda\lambda$ 6548,6584 lines are blended with H α in the G102 grism, so that our recorded H α fluxes are actually the combined fluxes of these three lines. Faisst et al. (2018) have derived an empirical estimate of the [NII]/H α ratio in G102 as a function of redshift and stellar mass for $0 < z < 2.7$ and $8.5 < \log(M_\star/M_\odot) < 11.0$. This empirical relation gives a fractional flux ranging from 5% to 45%. For the [OIII] $\lambda\lambda$ 4959,5007 lines, we simultaneously fit two Gaussians and the continuum, with an additional restriction that the flux ratio of the two Gaussians match the theoretical intensity ratio of 2.98 for the two lines derived in Storey and Zeippen (2000). The [OII] $\lambda\lambda$ 3727, 3729 doublet is too close to be resolved separately in FIGS spectra, and so is measured and reported together.

We ran this fitting procedure on each strong line in each PA that yielded a detection, and we averaged the fits for each line to obtain a final observed flux measurement. To get the flux error, we first estimated the error of the flux of each pixel from the standard deviation in the flux of the nearby continuum pixels. Then we integrated these errors with the line fit to produce the total error for the integrated line flux, rather than simply use the error in the fit parameters. This method typically produced a larger and more realistic flux error than relying on the derived error of the fit parameters, which was often artificially small resulting from the constraints on the fit.

We summarize the median properties of each type of strong line-emitter in Table 1. We give the full emission line catalog, including individual line fluxes, redshifts, continuum magnitudes, and equivalent widths in Table 2 in Appendix A. Figure 3 gives the redshift distribution of the lines, covering $0.3 < z < 2.1$, which is the full redshift coverage sampled by these three strong lines. Each line type’s redshift distribution is set by the wavelength coverage of the grism, though there is some overlap between H α and [OIII] and between [OIII] and [OII], as shown by the stacked bars. The bin sizes in the histogram scale with $0.03 \cdot (1 + z)$, so that the bin sizes roughly correspond to the photometric redshift error derived in Pharo et al. (2018), the redshift binning used in the environment analysis in §5. Comparing our redshift measurements to those in Pirzkal et al. (2018), we

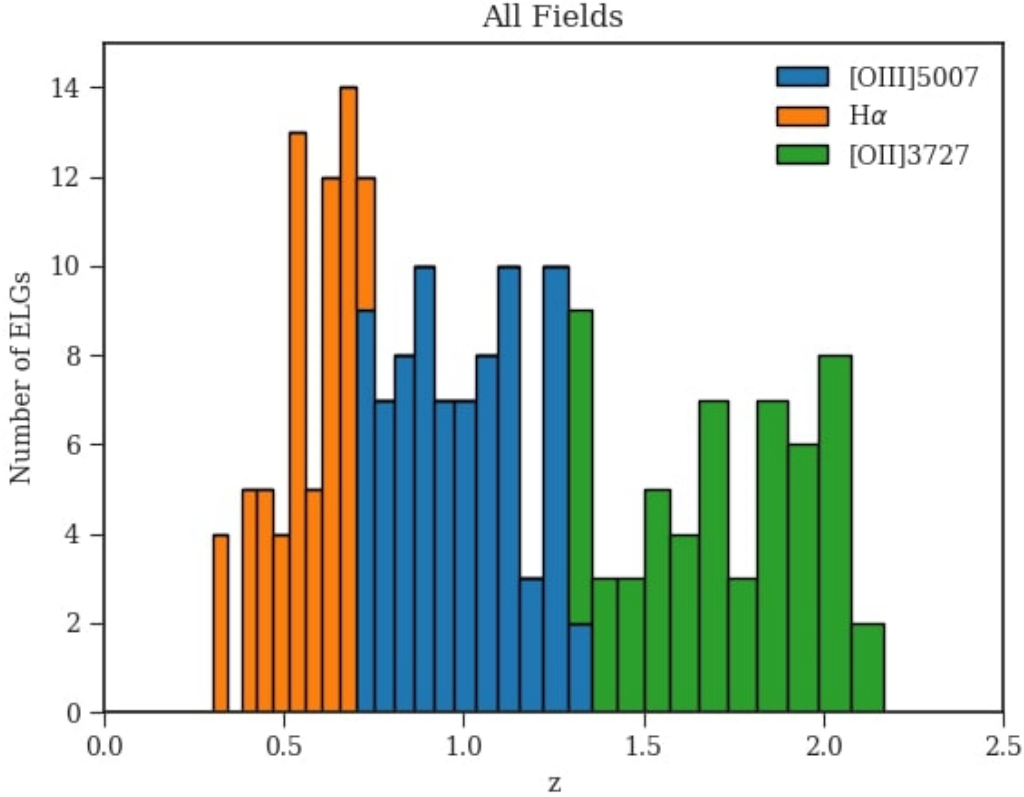


Figure 3. The distribution of identified ELGs by redshift. The histogram bins are scaled by $\Delta z = 0.03 \cdot (1+z)$ in order to encompass the expected redshift error derived from our redshift catalogs (though many individual objects have additional spectroscopic confirmation, and thus their real error is much lower). The bars of the histogram are colored according to the FIGS strong line ID, and redshift bins that contain more than one type of line in FIGS have stacked bars of two colors, so that the height of the stack is still the total number of objects in the bin.

find close agreement, with a median absolute difference of $|z_1 - z_2| = 0.001 \cdot (1 + z_1)$. Figure 4 shows a comparison as a function of redshift. We find 81 [OIII] emitters, more than each of the other two (71 H α , 56 [OII]), likely because it spans more volume coverage than the lower- z H α while having less redshift dimming than the higher- z [OII].

We also compared the line-derived redshifts with the matching sample of high-quality spec-zs described in §2.3.4, excluding the slitless grism surveys. We calculated $\Delta z / (1+z) = (z_{\text{FIGS}} - z_{\text{spec}}) / (1 + z_{\text{spec}})$. Figure 5 shows $\Delta z / (1+z)$ as a function of the galaxy half-light radius, taken from the catalogs in Skelton et al. (2014). There is no apparent dependence of the redshift accuracy on the size of the galaxy, and we find that 80% of the matched ELGs have $|\Delta z| / (1+z) \leq 0.0025$, the redshift change corresponding to one WFC3/G102 pixel at 10000 Å. 97% of the matched ELGs have $|\Delta z| / (1+z) \leq 0.005$, with just two outliers.

Figure 6 shows the distributions of some other properties of the ELG catalog. The leftmost panel gives the distribution of the observed line fluxes without correction for dust or redshift dimming for the three types of strong line emitter. This also shows the minimum line flux we were able to robustly measure, down to 10^{-17} erg cm $^{-2}$ s $^{-1}$. The faintest ELGs are dominated by [OII] λ 3727,

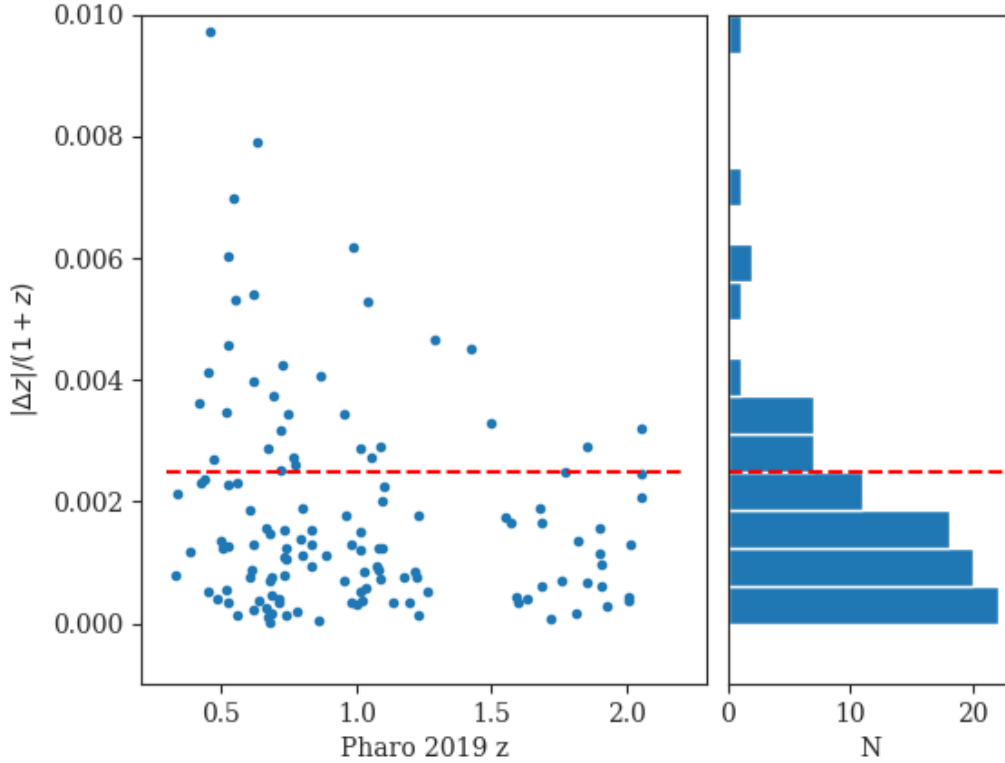


Figure 4. A comparison of line-derived redshifts between the 1D sample and matching 2D-selected ELGs from Pirzkal et al. (2018). The dashed line shows $|\Delta z|/(1+z) = 0.0025$. These offsets are within the scatter observed by Pirzkal et al. (2018) comparing derived redshifts between individual PAs, and thus could be explained by wavelength offsets between different line regions.

and the brightest are dominated by the lower-redshift $H\alpha$, with $[OIII]\lambda\lambda 4959, 5007$ spanning a broad range. Figure 6 also shows the distribution of F105W continuum magnitudes in the middle panel, showing that we detect ELGs for F105W up to 28 mag. Finally, the rightmost panel in Figure 6 gives the distribution of observed equivalent widths. Given the G102 resolution of $R = 210$, detections begin to drop off significantly for $EW < 30 \text{ \AA}$. Figure 7 compares the 1D ELG flux distribution with the same figure from Pirzkal et al. (2018). The distributions are very similar, though Pirzkal et al. (2018) find more high-flux ELGs and fewer faint-flux ELGs. This is possibly a result of the 2D method better detecting broad emission, and the 1D method detecting ELGs in fewer PAs.

5. ELG-OVERDENSITY RELATION

With a robust catalog of ELGs and their fluxes complete, in this section we use the catalog to probe ELG environments and explore how those environments relate to ELG properties.

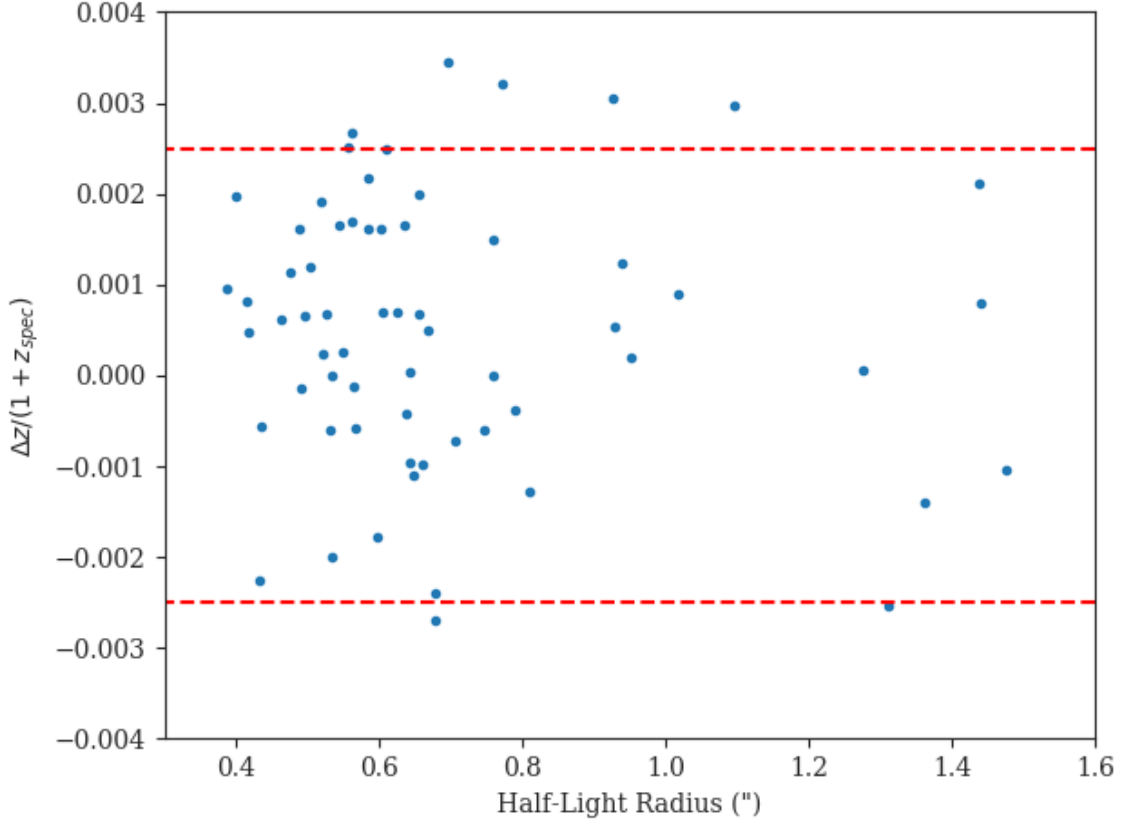


Figure 5. A comparison of the line-derived redshifts from this study and the matching spectroscopic redshift sample from §2.3.4 (excluding grism surveys) as a function of the half-light radius of the ELGs. The dashed lines show $\Delta z/(1 + z) = \pm 0.0025$, the redshift change corresponding to one WFC3/G102 grism element at 10000 Å. Two outliers with $\Delta z/(1 + z) = -0.065$ and -0.08 are not shown.

5.1. FIGS Overdensity Catalog

In [Pharo et al. \(2018\)](#), we used redshift catalogs derived from combined FIGS grism spectroscopy and broadband photometry to search for significant overdensities of galaxies in the FIGS fields. First, we divided each field into slices of redshift with $\Delta z = 0.03 \cdot (1 + z_{\min})$, where z_{\min} is the lower bound of the redshift slice. This Δz is based on the limiting accuracy of the [Pharo et al. \(2018\)](#) photometric redshift catalogs, which enabled the most significant detections of physically associated systems. In each redshift slice, we conducted a 7th-nearest-neighbor density search for a grid of points in the field. This is defined as:

$$n_7 = \frac{N}{\pi R_7^2} \quad (3)$$

where $N = 7$ and R_7 is the angular distance to the 7th-nearest galaxy in that redshift slice.

We then checked for points of significant overdensity with two different metrics. First, we calculated \mathcal{M} , the largest value of n_7 in the slice normalized to the slice's median n_7 . We also calculated \mathcal{S} , the peak nearest-neighbor density in the redshift slice divided by the standard deviation of densities in the adjacent redshift slices. We counted peaks with $\mathcal{M} = 10$ or $\mathcal{S} = 10$ as significant detections,

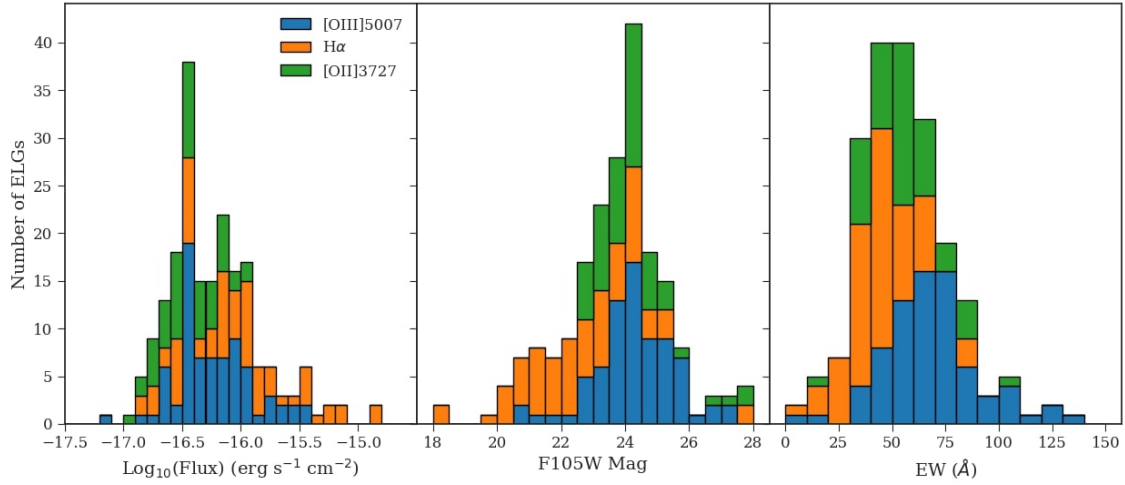


Figure 6. The distributions of ELG properties broken down by line ID. The histogram bars are colored according to the FIGS strong line ID, and bins that contain more than one type of line in FIGS have stacked bars of two or three colors. *Left:* The distribution of emission line fluxes given without correction for dust extinction. *Middle:* The distribution of identified ELGs by broadband F105W magnitude, in bins of 0.5 mag. *Right:* The distribution of observed equivalent widths (EW) in bins of 10 \AA . The median values for each line in each quantity are given in Table 1

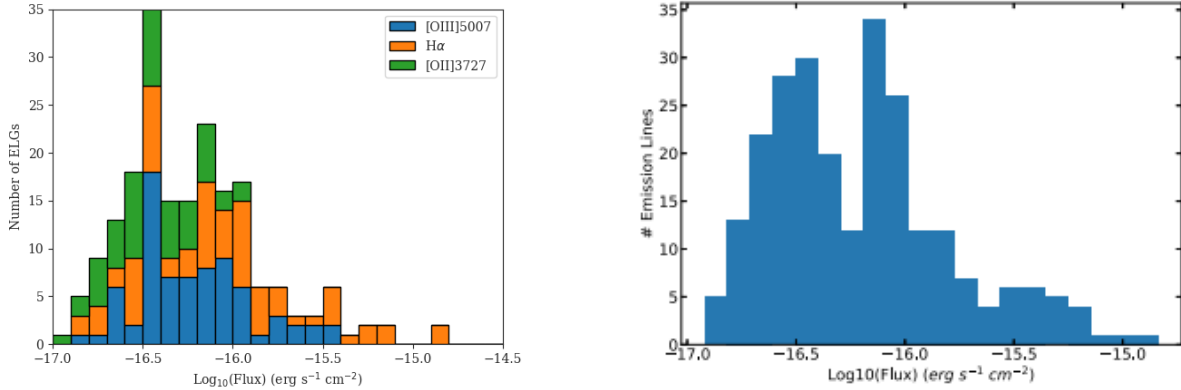


Figure 7. *Left:* The ELG flux distribution from this work. The axis limits have been truncated slightly to emphasize the comparison. The full flux range can be seen in Figure 6 above. *Right:* The ELG flux distribution from Pirzkal et al. (2018).

based on comparisons with other nearest-neighbor density searches (Spitler et al. 2012) and the values for spectroscopically identified clusters (see Pharo et al. 2018 for more detail). Across the 4 FIGS fields, we identified 24 such overdensities, as well as determining the R_7 values for individual FIGS galaxies. We make use of both the proximity to a detected overdensity and the R_7 distance of a galaxy to study environmental effects in the subsequent sections.

We also used the redshifts and angular separations of galaxies to determine the physical local surface density Σ for FIGS ELGs. For the purposes of this discussion, we will use terms such that field galaxies have $\Sigma < 6 \text{ Mpc}^{-2}$, rich fields have $6 < \Sigma < 10$, groups have $10 < \Sigma < 30$, and rich

groups have $\Sigma > 30$. These definitions are adapted from those used in Sobral et al. (2011), where they were based on derivations from correlation length studies of galaxies in Mo, Jing, and White (1996) and Yang et al. (2005). We measure ELGs in the field, rich field, and group density ranges, but not in the range of rich groups or above.

Figures 8 and 9 show the nearest-neighbor density plots of significant overdensities in the FIGS fields. The figures also show the locations of identified ELGs in each redshift slice, with triangles representing $H\alpha$ emitters, circles for [OIII] emitters, and stars for [OII] emitters. There appear to be several overdensities with associated ELGs, but this does not appear to be a consistent trend visually. The spectroscopically identified clusters at $z = 0.85$ and $z = 1.84$ have 2 and 3 ELGs in the same redshift slice, respectively. All but one of these ELGs appear near the overdensities, but not especially near the density peaks. Neither cluster appears to show an excess of identified ELGs compared to other slices. For the $z = 1.84$ cluster, this may seem in contradiction to the results of Tran et al. (2010), which found increased star formation activity near a cluster core at similar redshift. It's possible this is because the relatively faint [OII] is simply less complete compared to the lower-redshift sources, or because we do not find many galaxies with surface densities of $\Sigma \geq 20 \text{ Mpc}^{-2}$, the density at which Tran et al. (2010) begin to find the increased fraction of star-forming galaxies. We discuss the SFRs themselves and their implications in §5.3-5.5.

5.2. The R_7 Distribution

In order to systematically study a possible relationship between strong line emission and galaxy environment, we first looked at the R_7 distance for both ELGs and regular galaxies. If ELGs have a preferred relationship with overdensities, then the distribution of R_7 distances could be distinct from non-emitting galaxies, since, for example, a preference for ELGs to be close to overdensities should result in a distribution that peaks more at low R_7 .

Figure 10 shows the probability density distributions of R_7 distances for ELGs compared to the whole set of galaxies in our redshift catalog. The distributions are broken down into six subsamples, in order to make meaningful comparisons of distance and stellar mass: first, by redshift ranges corresponding to the three strong emitters, and then by bright and faint F105W continuum magnitudes as a proxy for mass. To judge the significance of the differences between a given pair of distributions, we applied a two-sample Kolmogorov-Smirnov (KS) test, a statistical test to determine whether two underlying one-dimensional probability distributions differ, to each subsample pair. The test produces a p-value determined by the sizes and differences of the two distributions, and this p-value gives the level of significance at which the two may be considered distinct. A lower p-value corresponds to a more significant determination that the two distributions are different.

This test showed no significant difference in the R_7 distribution of $H\alpha$ emitters compared to other galaxies in either the bright or faint bins. For [OIII] $\lambda\lambda 4959, 5007$ emitters, the test does find a significant difference in distributions for both the bright ($p = 3 \cdot 10^{-7}$) and faint ($p = 0.02$) bins, with [OIII] $\lambda\lambda 4959, 5007$ emitters having a higher probability of appearing at mid-range R_7 distances compared to other galaxies. For [OII] $\lambda 3727$ emitters, the test finds a significant difference only in the bright bin ($p = 0.002$). This measurement for [OIII] supports previous studies that find line-emitters preferentially at intermediate distances around clusters (Darvish et al. 2014) at $z \simeq 1$. We explore this result in more detail in §5.5.

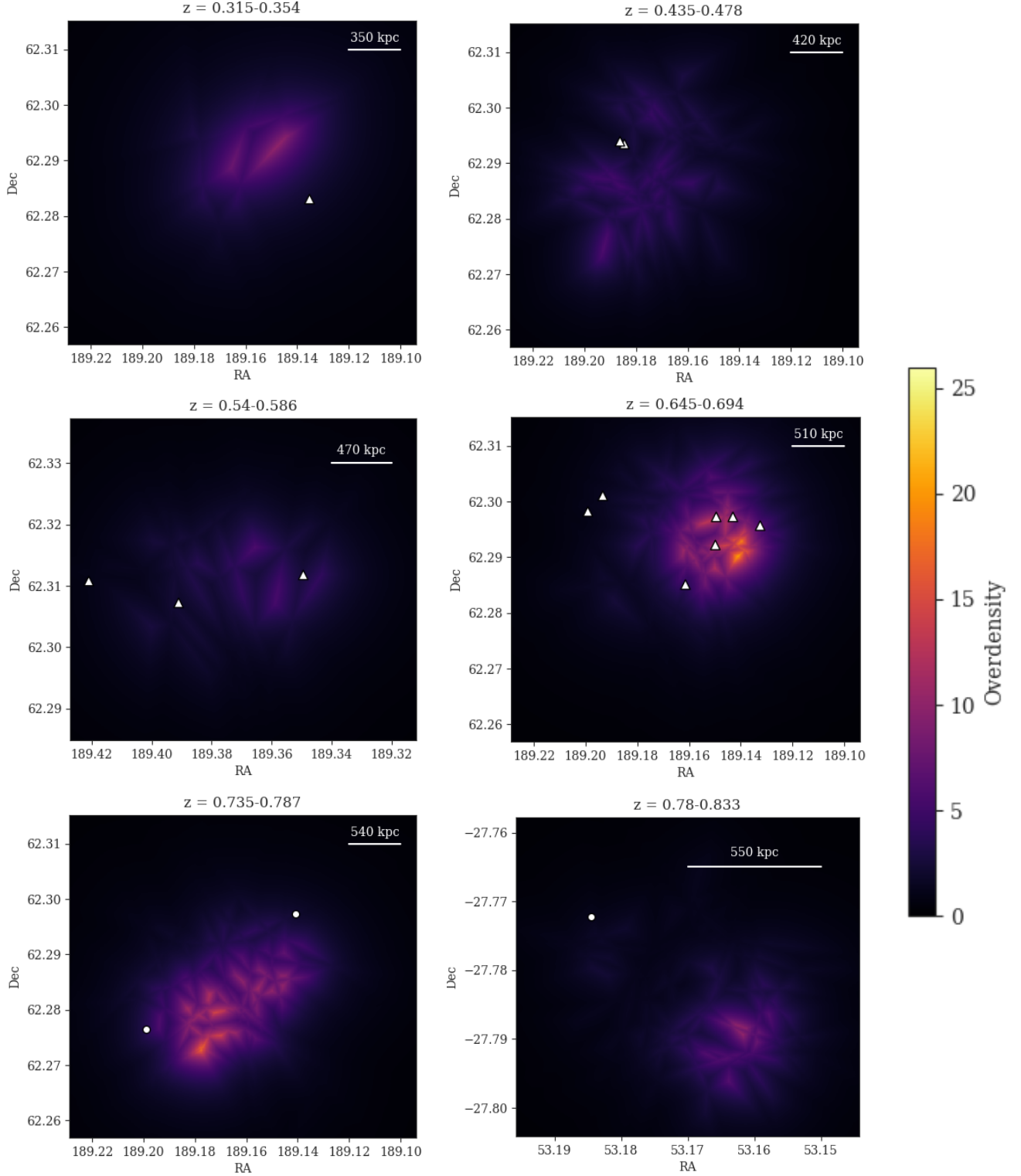


Figure 8. Example overdensities in the FIGS fields. Each image, organized from low redshift to high, shows a redshift slice where a significant overdensity was detected in [Pharo et al. \(2018\)](#), and is shaded according to the local overdensity measure, which is the ratio of the local nearest neighbor density to the median density of the redshift slice. The locations of ELGs are marked with white points, with triangles representing $H\alpha$ emitters, circles for $[OIII]$ emitters, and stars for $[OII]$ emitters.

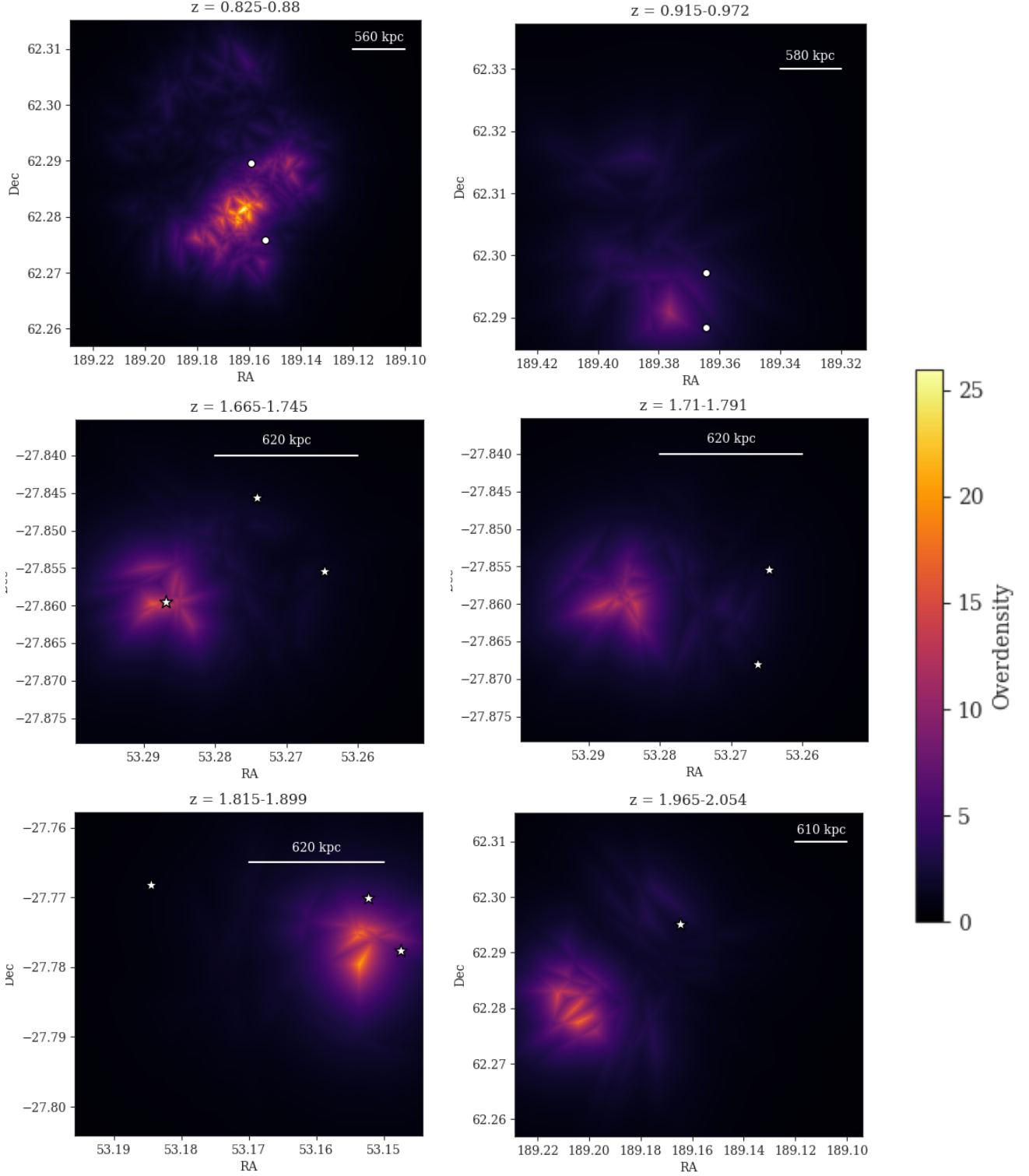


Figure 9. More overdensities in the FIGS fields, including the known clusters. Each image, organized from low redshift to high, shows a redshift slice where a significant overdensity was detected in [Pharo et al. \(2018\)](#), and is shaded according to the local overdensity measure, which is the ratio of the local nearest neighbor density to the median density of the redshift slice. The locations of ELGs are marked with white points, with triangles representing $H\alpha$ emitters, circles for $[OIII]$ emitters, and stars for $[OII]$ emitters.

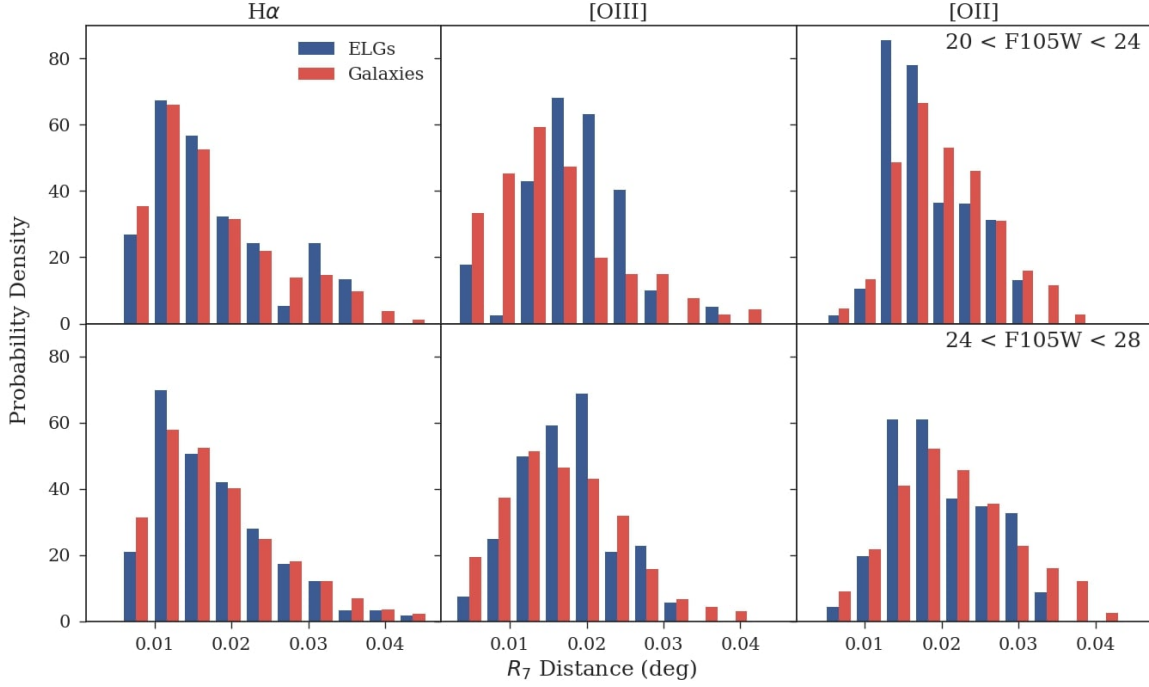


Figure 10. The probability density distributions of R_7 distances, separated into bins of redshift and F105W continuum magnitude, for ELGs (blue) and all galaxies (red) in a given magnitude-redshift bin. The first column uses $0.3 < z < 0.8$, corresponding to $H\alpha$ emission. The middle column uses $0.8 < z < 1.3$ ($[OIII]\lambda\lambda 4959, 5007$), and the right column uses $1.3 < z < 2.1$ ($[OII]\lambda 3727$). The top row compares ELGs and galaxies with $20 < F105W < 24$ mag (bright). The bottom row compares ELGs and galaxies with $24 < F105W < 28$ mag (faint). For each distribution pair, we applied a two-sample K-S test to determine whether the distributions differed significantly. Both the bright and the faint $H\alpha$ distributions are indistinguishable from the distributions of galaxies. The distributions of the $[OIII]\lambda\lambda 4959, 5007$ emitters do differ significantly ($p = 3 \cdot 10^{-7}$ for the bright distribution, $p = 0.02$ for the faint), with the $[OIII]\lambda\lambda 4959, 5007$ emitters found preferentially at middling R_7 values as opposed to low R_7 . The $[OII]\lambda 3727$ distribution differs significantly only in the bright sample ($p = 0.02$).

5.3. Measuring Star Formation

Studying the R_7 distribution by itself gives insight into only the relationship between the locations of ELGs and of overdensities, while ignoring the other properties of the ELGs. With the flux catalog, we were also able to investigate how an ELG’s environment might influence its emission line luminosity and recent star formation rate.

To account for the effects of dust extinction in measuring the SFR, we used a dust calibration developed by Sobral et al. (2012) using rest-frame $u-z$ colors. The calibration was developed and tested using $H\alpha$ and $[OII]$ emitters at $z = 0.1$ and $z = 1.47$. It is given by

$$A_{H\alpha} = -0.092(u - z)^3 + 0.671(u - z)^2 - 0.952(u - z) + 0.875 \quad (4)$$

Sobral et al. (2012) find that this relation holds across redshift epochs, covering most of the redshift range of our sample and for both kinds of emitters. To convert the $A_{H\alpha}$ calculation to $A_{[OIII]}$ and $A_{[OII]}$, we applied the Calzetti et al. (2000) reddening law. For the few objects for which one of rest-frame u or z was unavailable, we assigned the median reddening value from the rest of the sample.

We also measured $A_{H\alpha}$ using the stellar mass dust parameterization developed in [Garn and Best \(2010\)](#) (see §5.4 for discussion of stellar masses). This typically produced similar dust measures to the color calibration, with a divergence at masses greater than $10.5 \log(M_{\odot})$, as was also observed in [Ramraj et al. \(2017\)](#). Such objects make up a very small fraction of our ELG sample, so this doesn't change any overall trends.

We calculated SFRs for the ELGs using the following equations:

$$\text{SFR}_{H\alpha} (M_{\odot} \text{ yr}^{-1}) = 7.9 \times 10^{-42} L(H\alpha) \text{ (erg s}^{-1}\text{)} \quad (5)$$

$$\text{SFR}_{[\text{OII}]} (M_{\odot} \text{ yr}^{-1}) = 1.4 \pm 0.4 \times 10^{-41} L([\text{OII}]) \text{ (erg s}^{-1}\text{)} \quad (6)$$

$$\text{SFR}_{[\text{OIII}]} (M_{\odot} \text{ yr}^{-1}) = 6.4 \pm 4.0 \times 10^{-42} L([\text{OIII}]) \text{ (erg s}^{-1}\text{)} \quad (7)$$

Equations 5 and 6 are calibrations from [Kennicutt \(1998\)](#), derived with a Salpeter IMF. Equation 7 was derived by [Straughn et al. \(2009\)](#) using [OIII]- $H\alpha$ ratios from star-forming galaxy knots where both emission lines were present.

5.4. Environment and the SSFR-Mass Relation

We obtained stellar masses for our ELG sample by applying our EAZY SED catalogs to the SED fitting code FAST ([Kriek et al. 2009](#)), using a [Chabrier \(2003\)](#) initial mass function, [Bruzual and Charlot \(2003\)](#) templates, and an exponential star formation history. We used spec-zs for the fits where high-quality matching redshifts were available in our compilation, and used the best-fit photometric redshift otherwise. We checked the results for the GS1 field against the GOODS-South catalogs compiled by [Santini et al. \(2015\)](#), which largely exclude our GS2 parallel field. For the galaxies with existing measurements, we found our mass results consistent with the [Santini et al. \(2015\)](#) catalogs, with a median difference of less than 0.1 dex. For the other fields, we checked against matching masses from [Skelton et al. \(2014\)](#), and found a similar level of agreement.

With the stellar masses calculated, we were able to determine each ELG's SFR per stellar mass, or specific star formation rate (SSFR). The relation between SSFR and mass for star forming galaxies is typically called the galaxy main sequence, and it suggests an evolution of star formation with redshift and stellar mass ([Noeske et al. 2007](#)). In star forming galaxies, as redshift decreases, ongoing star formation builds up increased stellar mass, and as this happens SSFRs decline as the galaxies exhaust their supplies of gas.

This smooth relation doesn't account for cases of rapid quenching, and does not address the influence of environment on how galaxies evolve. In Figure 11, we show the SSFR as a function of the stellar mass, and compare our ELGs to the results from [Noeske et al. \(2007\)](#), who measured this in four redshift bins up to $z = 1.1$. We show the best-fit staged-tau models of star formation history from [Noeske et al. \(2007\)](#) in the redshift bins most closely matching our $H\alpha$ and [OIII] emitters (the [OII] sample is at too high a redshift), and find that our ELGs typically have higher SSFR for a given stellar mass.

This may be due to the luminosity limit of our sample. Since the limiting luminosity is redshift dependent, we determined the lower-bound SSFR based on the lower and upper redshift limits of each ELG sample. We show these lines in Figure 11. For [OIII] and [OII], the limiting SSFRs are relatively high, indicating that we are likely sampling the upper region of the galaxy main sequence.

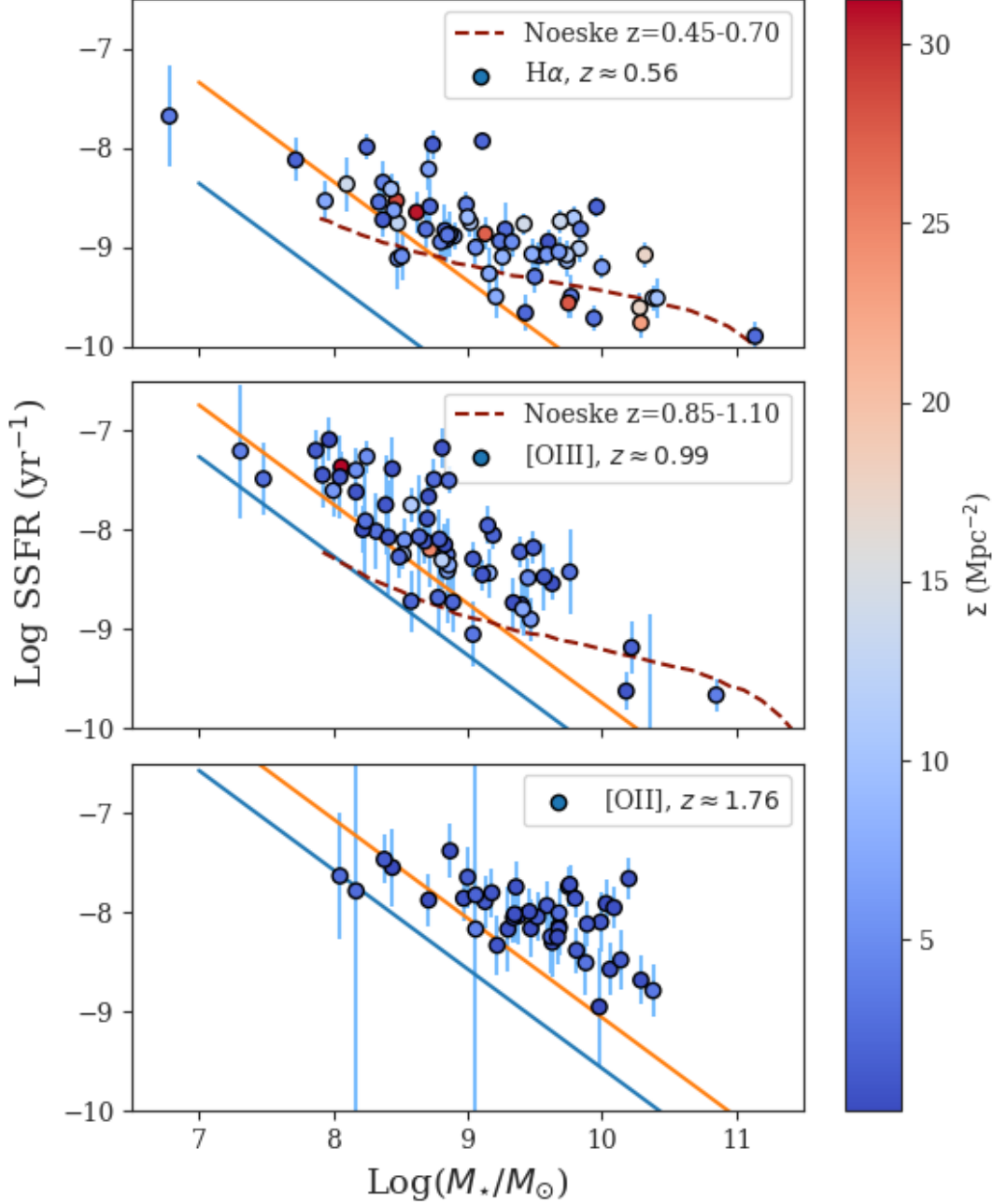


Figure 11. The specific star formation rate (SSFR) as a function of the stellar mass. The ELGs are given by colored circles ($H\alpha$, top panel; $[O\text{ III}]\lambda\lambda 4959, 5007$, middle; $[O\text{ II}]\lambda 3727$, bottom), and are shaded by their value of Σ , the local density of galaxies (see §5.5 for description). The median z for each panel’s FIGS subsample is given in the panel legend. Each panel also shows two lines of completeness (blue and orange solid lines), derived from the limiting line flux we measured (see Figure 6), and the minimum and maximum possible redshifts for each line. There is no clear trend between Σ and a galaxy’s position on the SSFR-mass relation. The red dashed curves are the best-fit staged-tau models from Noeske et al. (2007). Our ELGs typically sit at higher SSFR for a given stellar mass compared to the models at comparable redshift, but this is likely due to the flux limitations of our sample.

We were still able to investigate the possible environmental effects on the main sequence, especially for $H\alpha$, where we probe the main sequence most closely. In Figure 11, we also show each galaxy’s local surface density Σ . There is no significant relationship between either Σ and the stellar mass or Σ and position on the SSFR-mass relation to the densities probed, which at most get only as dense as galaxy groups ($10 < \Sigma < 30$, as defined in §5.1.). The same holds for the ELGs’ R_7 measurements. This suggests that environmental effects do not play a systematic role in either quenching or triggering star formation, since they do not appear to disrupt the smooth star formation relation of the main sequence.

5.5. Line Luminosity and Clustering

We also studied the relationship between emission line strength and galaxy clustering more directly. First, we used the galaxies’ redshifts and angular separations to compute the local physical surface density Σ in units of Mpc^{-2} for each ELG. Then, we split the sample of ELGs into two subsamples: those located in a redshift slice where a significant overdensity is detected (“In OD”), and those in a redshift slice with no overdensity detection (“No OD”). By looking at these subsamples, we could check if ELG properties differ for galaxies near a range of peak densities. This also gives us a subsample to compare directly to studies focused only on known clusters. This result can be seen in Figure 12, which shows the line luminosity as a function of Σ for $H\alpha$, [OIII], and [OII] emitters. In each panel, the horizontal dashed lines give the median line luminosity for each subsample, and the vertical dashed lines give the median Σ . We inspected the SFR- Σ and SSFR- Σ relations as well (see Figure 14), and the distributions remained essentially unchanged for each emitter. Thus, for this discussion we will refer simply to the L- Σ relation shown in Figure 12, as that requires the fewest additional assumptions.

The $H\alpha$ L- Σ distribution (top panel) shows little indication of a preferred relationship with density. Even in the OD slices, $H\alpha$ emitters are found at a range of local densities, and with a range of luminosity values. The median luminosity for emitters near overdensities is 0.3 dex higher than for those in non-OD slices, which is about twice the typical error size for the $H\alpha$ emitters. Figure 13 shows the same L- Σ relation with the points shaded by SSFR and stellar mass, but no clear trends with density emerge.

In Figure 14, we compared the derived $H\alpha$ SFRs from this luminosity sample to a narrowband-selected sample of star-forming ($\text{SFR} > 3M_{\odot} \text{ yr}^{-1}$) $H\alpha$ emitters at $z = 0.845$ (Sobral et al. 2011), using the same SFR diagnostic. Our distribution differs from the result in Sobral et al. (2011), which shows SFR increasing with density up to $\Sigma \simeq 50 \text{ Mpc}^{-2}$. The discrepancy may be at least partially explained by their selection of $\text{SFR} > 3M_{\odot} \text{ yr}^{-1}$ emitters, which would exclude much of our sample. SFR measurements of FIGS ELGs go down to $0.1M_{\odot} \text{ yr}^{-1}$, but our sample probes to lower stellar mass, yielding comparable SSFRs. Nevertheless, this does limit the utility of a comparison with the Sobral et al. (2011) results. Darvish et al. (2014) conducted a similar study down to a limit of $\text{SFR} > 1.5M_{\odot} \text{ yr}^{-1}$, and finds only a small difference in median SFR between field and cluster galaxies. However, Darvish et al. (2014) also find that at intermediate densities, comparable to the rich field or group densities described earlier, a higher fraction of galaxies exhibit star formation compared to fields and rich clusters.

To get a broader sense of environmental effects at different redshifts, we need to look at non-narrowband studies. Grützbauch et al. (2011a) found a weak correlation between overdensity and $U-B$ color, used as a proxy for star formation, using data from the POWIR and DEEP2 surveys. Their

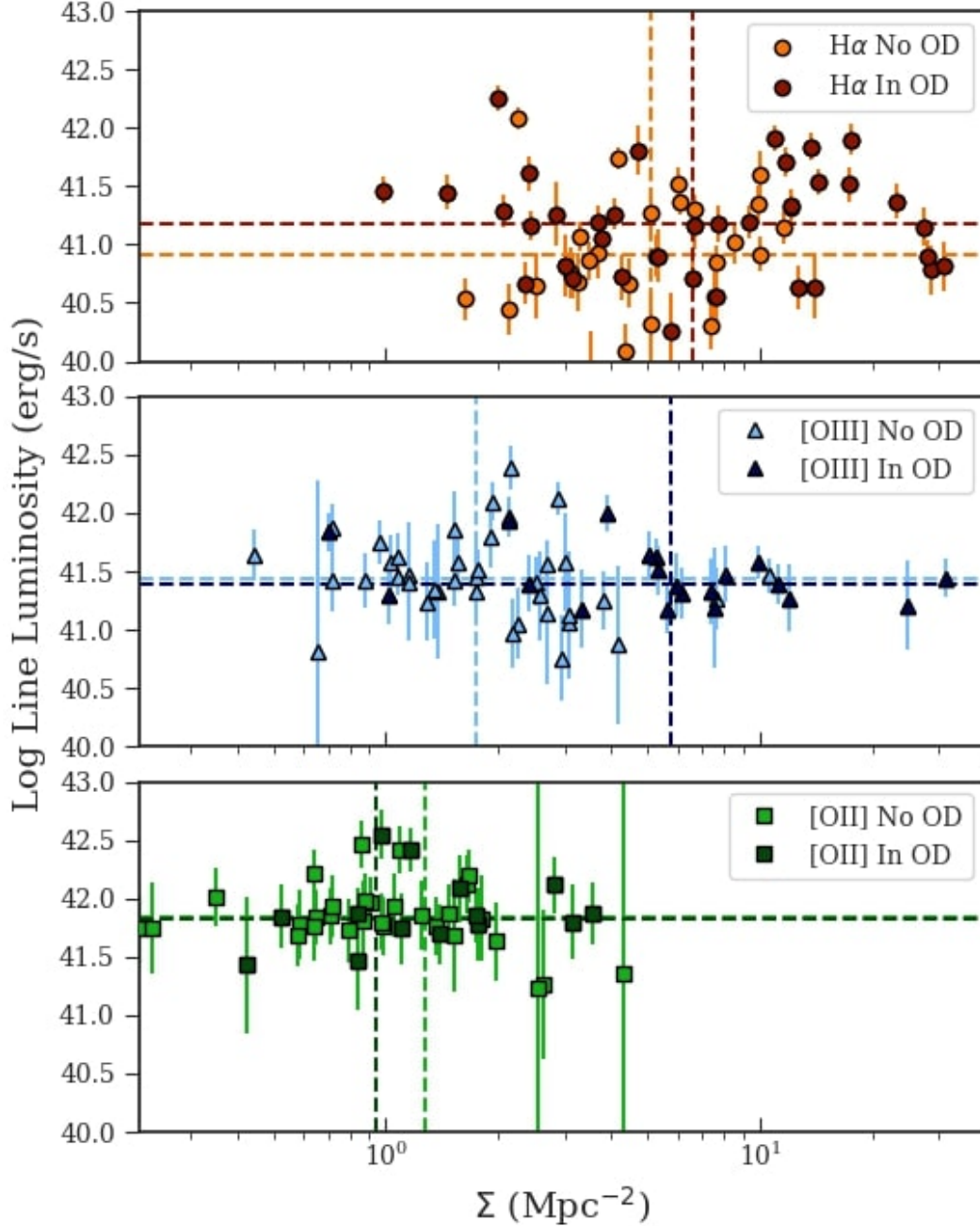


Figure 12. The line luminosity as a function of surface density for FIGS ELGs. The ELGs are given by orange circles (H α , top panel), blue triangles ([O III] $\lambda\lambda 4959, 5007$, middle), and green Xs ([O II] $\lambda 3727$, bottom). Each panel contains two subsamples: emitters found in redshift slices without a significant overdensity detection ("No OD"; lighter colors), and emitters found in slices with a significant detection ("In OD"; darker colors). The median luminosity and Σ values for each subsample are given by the horizontal and vertical dashed lines. This shows a substantial difference in the locations of [O III] emitters depending on the proximity of an overdensity: in redshift slices with an overdensity, the [O III] emitters are much more likely to be found at densities corresponding to group outskirts.

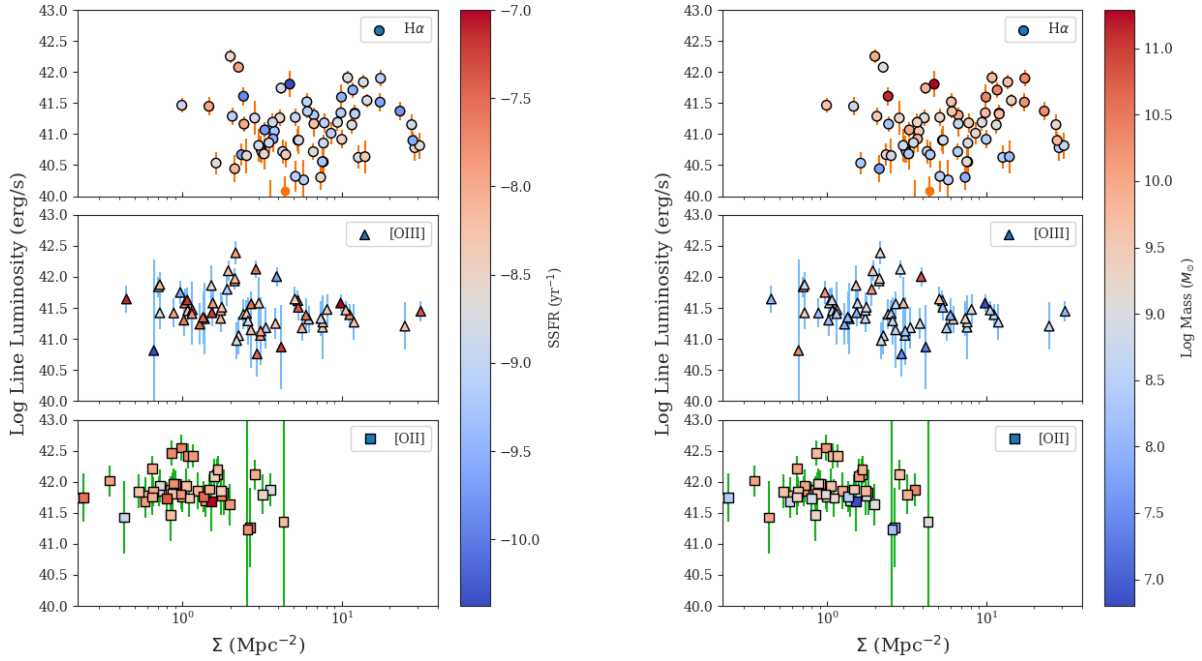


Figure 13. Left: The L- Σ distribution colored by SSFR. Right: The L- Σ distribution colored by stellar mass.

study showed declining star formation with increasing density at $0.4 \leq z \leq 0.7$, roughly matching the redshift range of our H α emitters, which becomes a flat relation for $0.85 \leq z \leq 1$. In their paper, they do not attempt to convert the color to SFR or SSFR, but in Grützbauch et al. (2011c) the change in observed color is shown to correlate with a half-dex decrease in SSFR at $1.5 < z < 2$. Grützbauch et al. (2011a) also measure these effects in terms of overdensity, not physical density, so a direct comparison with our results and that of Sobral et al. (2011) is not possible. However, their largest overdensity bin corresponds to the value of our overdensity cutoff; in this case, one might expect to see a decline in H α line luminosity among those galaxies marked "In OD," but no such decline is apparent. The result of Grützbauch et al. (2011a) was limited to stellar masses down to only $\log(M_*/M_\odot) > 10.25$, so they may not have detected the low-luminosity scatter we observe at low Σ , while observing a decline in high SFR as Σ increases.

Scoville et al. (2013) studied NUV-continuum-derived SFRs versus density in redshift slices up to $z < 3$ in COSMOS, finding a flat SFR- Σ relationship for $0.8 < z < 2$. Scoville et al. (2013) studied the SFR- Σ relation in terms of density percentiles, of which the highest encompassed $\Sigma > 10 \text{ Mpc}^{-2}$ and the lowest $\Sigma < 0.1 \text{ Mpc}^{-2}$. At $z < 1$, they measure a flat relationship up to Σ of a few for the lower and medium density percentiles, after which the SFR declines with increasing density in the highest percentiles. At $0.35 < z < 0.6$, the redshift bin most comparable to our H α sample, the decline is notable in only the highest-density bin, where the median SFR drops from $1.5M_\odot$ to $0.3M_\odot$. We do not observe this drop in the line luminosity (or in dust-corrected SFRs), but the high-density percentile from Scoville et al. (2013) includes densities up to $\sim 100 \text{ Mpc}^{-2}$, and perhaps the drop in SFR is concentrated in these very high density sources. If so, it could be the case that we do not

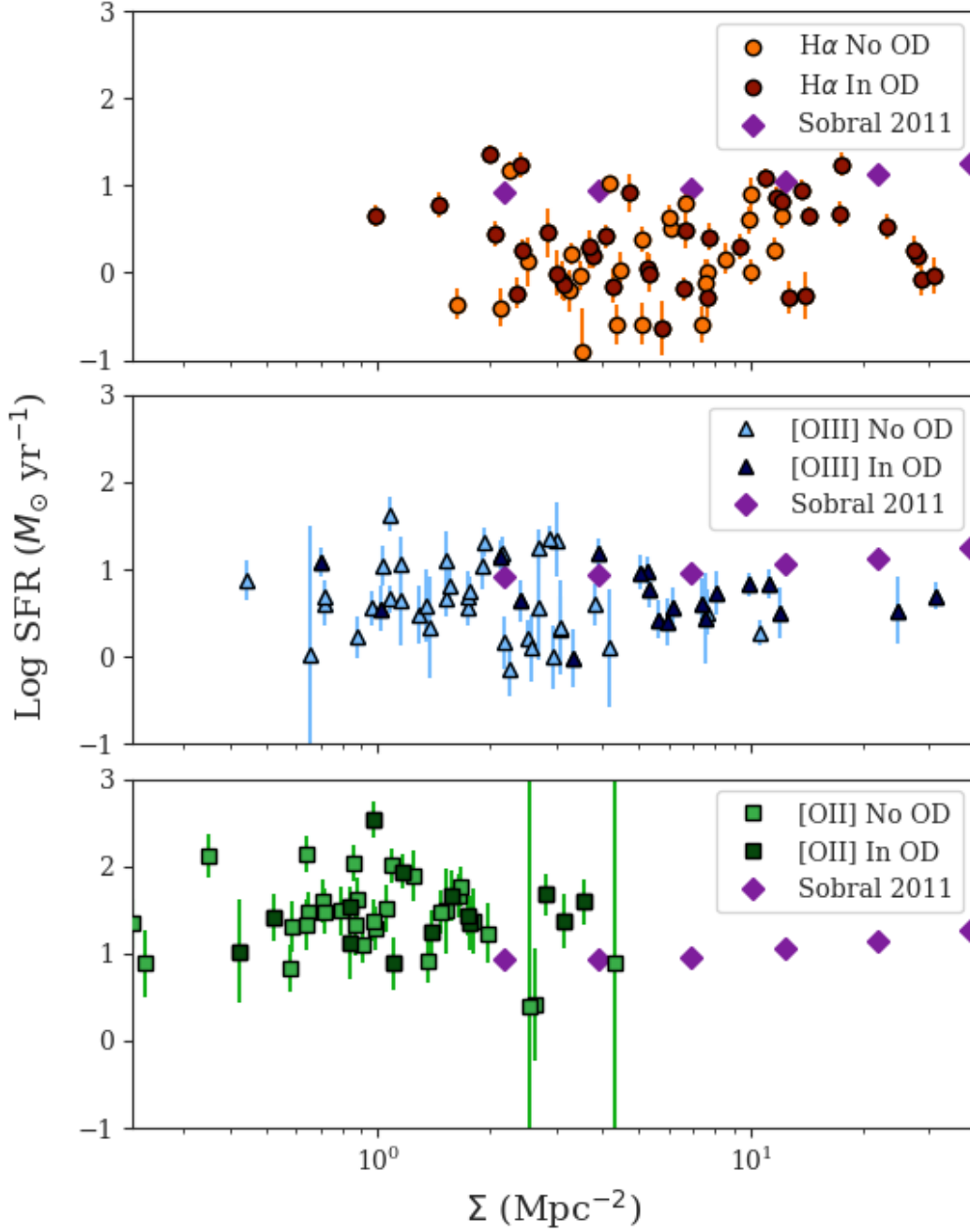


Figure 14. The SFR- Σ relation. The ELGs are given by orange circles (H α , top panel), blue triangles ([O III] $\lambda\lambda 4959, 5007$, middle), and green Xs ([OII] $\lambda 3727$, bottom). Each panel contains two subsamples: emitters found in redshift slices without a significant overdensity detection (“No OD”; lighter colors), and emitters found in slices with a significant detection (“In OD”; darker colors). Median SFR bins from Sobral et al. (2011) are shown with purple diamonds.

detect ELGs at such high density because their star formation has dropped too low, leading to fainter (or no) line emission. The trends from [Scoville et al. \(2013\)](#), combined with the results of [Darvish et al. \(2014\)](#), could suggest a transition period from peak star formation and merger interactions at $z \simeq 2$ ([Madau and Dickinson 2014](#)) to the local universe. After the merger peak, higher-density environments may have already quenched star formation in local galaxies through strangulation or ram-pressure stripping ([Muzzin et al. 2012; Muzzin et al. 2014](#)), depleting their reserves of star-forming material and increasingly relegating star formation to intermediate and field densities. This could be the case with our $H\alpha$ sample, if the lack of high- Σ emitters is due to the depletion of star formation at high density.

The $[\text{OIII}]\lambda\lambda 4959, 5007$ L- Σ distribution (middle panel) shows an essentially flat relationship, with high scatter at the lowest densities. In slices with an overdensity, the emitters we find are much more likely to occupy densities in the range $5 < \Sigma < 15$, with 12 out of 20 emitters in OD slices found in this region. The median Σ is a factor of a few higher for $[\text{OIII}]$ emitters in overdensity slices compared to those not near overdensities. This is distinct from the $H\alpha$ emitters, which don't seem to have a distinct density preference when near overdensities.

The density where the $[\text{OIII}]$ emitters are preferentially located corresponds to the rich fields and galaxy groups at the outskirts of a denser cluster, corroborating what we see in Figure 10. This result also matches the findings in [Grützbauch et al. \(2011a\)](#) and [Scoville et al. \(2013\)](#), as we find a flat SFR-density relationship at $0.8 < z < 1.3$. We do not see the higher SFR at intermediate density that [Darvish et al. \(2014\)](#) measured, but our results do corroborate their finding of a higher fraction of star-forming galaxies at those densities. Compared to the $H\alpha$ distribution, which shows emitters at all density ranges near overdensities, this could suggest an evolution with redshift in the preferred locations of group star forming galaxies near overdensities, which are found nearer to rich group densities among the FIGS $H\alpha$ emitters.

The $[\text{OII}]\lambda 3727$ SFR- Σ distribution (bottom panel) shows no relationship, with all the emitters found at low Σ . This is likely due in part to the limits of our overdensity search near $z \simeq 2$, where our sample of fainter galaxies is less complete (see §5.4 for further discussion). One can see this effect in the range of SFRs calculated for the $[\text{OII}]$ emitters, which is restricted to much higher star formation than the other two samples. Of the 24 overdensity candidates, only 4 are in the redshift range where we might find $[\text{OII}]$, and these are of lesser significance and based on fewer galaxies compared to the overdensity candidates at lower redshift. These caveats aside, this could suggest that at higher redshift, field galaxies exhibit higher star formation, at least among the brightest galaxies. [Patel et al. \(2009\)](#) found in a study of $z \simeq 0.8$ galaxies with $\log(M_*/M_\odot) > 10$ that specific star formation (SFR per stellar mass) declined with increasing density. Since the limits of our completeness at this redshift selects more massive galaxies, this could indeed explain our findings.

5.6. Line Emission and Galaxy Pairs

We also investigated the behavior of ELGs with close companion galaxies, in order to study overdensities and environmental effects on a smaller scale. If nebular emission and related star formation are triggered by interactions with companion galaxies ([Kennicutt et al. 1987; Alonso et al. 2004](#)), then we could observe a difference in the number of nearby galaxies between ELGs and galaxies. [Ellison et al. \(2010\)](#) studied the effects on environment of interacting galaxy pairs selected from SDSS DR4, finding a small increase in SSFR for the closest pairs at low Σ relative to both more distant pairs and pairs found at higher galaxy densities. Their distance criterion for identifying a pair required a

projected distance of $R_p < 80 \times h_{70}^{-1}$ kpc between the two galaxies. Using this projected distance as the range for possible companions, we find that the fractions of ELGs (31%) and non-ELGs (32%) that form a near pair are essentially the same. Kocevski et al. (2012) used a much narrower allowable pair range (12 kpc) to search for interactions near AGN hosts. Applying this much stricter cut yields a 3% pair rate in both ELGs and non-ELGs, suggesting that line emission and star formation are not necessarily directly connected to the presence of a nearby companion.

6. CONCLUSIONS

In this paper, we used deep NIR slitless spectroscopy to conduct an automated search for emission line galaxies. Using our continuum-subtracted peak-finding technique, we detected and identified 208 $H\alpha$ 6563, [OIII] $\lambda\lambda$ 4959,5007, and [OII] λ 3727 emitters in the four FIGS fields. For these emitters, we provide a robust catalog with integrated line fluxes, flux errors, line-derived redshifts, and observed equivalent widths. We measure line fluxes down to 10^{-17} erg cm $^{-2}$ s $^{-1}$ for objects with continuum magnitudes up to F105W < 28 mag. We compare line-derived redshifts to high-quality spectroscopic redshifts and find that 80% of ELG redshifts match the spec-zs within $\Delta z = \pm 0.0025$, the width of the WFC3-G102 grism element. We find no dependence of this redshift accuracy on galaxy size.

We use the flux catalog to derive SFRs and the local surface densities of galaxies, which we use to search for trends in the SFR-density relation. We find that [O III] emitters are preferentially found at intermediate densities in the outer regions of galaxy groups, as shown in Figure 10, corroborating a finding at similar redshifts. When placing our sample on the SSFR-mass relation, we find higher SSFR per stellar mass compared to other studies at comparable redshift, though this is largely explained by limits on measured line flux. We find that SFR has no significant dependence on increasing local galaxy surface density for $0.3 < z < 0.8$ $H\alpha$ emitters and for $0.8 < z < 1.3$ [OIII] emitters, as shown in Figure 12. We find no indication that environment influences a galaxy’s location in this relation. A study of close galaxy pairs finds that ELGs are not more or less likely to have a close companion than non-ELGs. We compare our results with other environment studies after the peak in cosmic star formation at $z \simeq 2$ (Madau and Dickinson 2014), which show a variety of possible relations across different redshifts. We observe a difference in the preferred location of rich field and group ELGs near overdensities, from a preference for rich field densities at $z \simeq 1$ to no preference between field and group densities at $z \simeq 0.5$. We do not find ELGs at the high surface densities common to rich groups or clusters, which could be due to low star formation at those densities.

We would like to thank the referee for many thoughtful comments and helpful suggestions. This work is based on observations made with the NASA/ESA Hubble Space Telescope, obtained from the Data Archive at the Space Telescope Science Institute, which is operated by the Association of Universities for Research in Astronomy, Inc., under NASA contract NAS 5-26555. These observations are associated with program #13779. Support for program #13779 was provided by NASA through a grant from the Space Telescope Science Institute, which is operated by the Association of Universities for Research in Astronomy, Inc., under NASA contract NAS5-26555. A.C. acknowledges the grants ASI n.I/023/12/0 “Attivit relative alla fase B2/C per la missione Euclid” and PRIN MIUR 2015 “Cosmology and Fundamental Physics:illuminating the Dark Universe with Euclid.”

REFERENCES

- Alonso, M. S., Tissera, P. B., Coldwell, G., Lambas, D. G., 2004, MNRAS, 352, 1081
- Atek, H., Malkan, M., McCarthy, P., et al. 2010, ApJ, 723, 104
- Bacon, R., Accardo, M., Adjali, L., et al. 2010, Proc. SPIE, 7735, 773508
- Bacon, R., Piqueras, L., Conseil, S., Richard, J., & Shepherd, M. 2016, MPDAF: MUSE Python Data Analysis Framework, Astrophysics Source Code Library, ascl:1611.003
- Bacon, R., Conseil, S., Mary, D., et al. 2017, A&A, 608, A1
- Balestra, I., Mainieri, V., Popesso, P., et al. 2010, A&A, 512, 12
- Balogh, M., Eke, V., Miller, C., et al. 2004, MNRAS, 348, 1355
- Barger, A. J., Cowie, L. L., and Wang, W.-H., 2008, ApJ, 689, 687
- Boroson, T. A., Salzer, J. J., & Trotter, A. 1993, ApJ, 412, 524
- Brammer, G. B., Van Dokkum, P. G., Franx, M., et al. 2012, ApJS, 200, 13
- Bruzual, G., & Charlot, S. 2003, MNRAS, 344, 1000
- Calzetti et al. 1994, ApJ, 429, 582
- Calzetti D., Armus L., Bohlin R. C., Kinney A. L., Koornneef J., StorchiBergmann T., 2000, ApJ, 533, 682
- Chabrier, G. 2003, PASP, 115, 763
- Cooke, J., Wolfe, A. M., Gawiser, E., & Prochaska, J. K., 2006, ApJ, 652, 994
- Cooper, M. C., Newman, J. A., Weiner, B. J., et al. 2008, MNRAS, 383, 1058
- Cooper, M. C., Aird, J. A., Coil, A. L., et al. 2011, ApJS, 193, 14
- Cooper, M. C., Yan, R., Dickinson, M., et al. 2012, MNRAS, 425, 2116
- Coughlin, A., Rhoads, J. E., Malhotra, S. et al. 2018, ApJ, 858, 96
- Darvish, B., Sobral, D., Mobasher, B., et al. 2014, ApJ, 796, 51
- Djorgovski, S., Spinrad, H., McCarthy, P., & Strauss, M. A. 1985, ApJL, 299, L1
- Dressler, A. 1980, ApJ, 236, 351
- Elbaz, D., Daddi, E., Le Borgne, D., et al. 2007, A&A, 468, 33
- Ellison, S. L., Patton, D. R., Simard, L., et al. 2010, MNRAS, 407, 1514
- Faisst, A. L., Masters, D., Wang, Y., et al. 2018, ApJ, 855, 132
- Ferreras, I., Pasquali, A., Malhotra, S., et al. 2009, ApJ, 706, 158
- Ferreras, I., Trujillo, I., Mármol-Queraltó, E., et al. 2014, MNRAS, 444, 906
- Finkelstein, S., Papovich, C., Dickinson, M., et al. 2013, Nature, 502, 524
- Garn T., Best P. N., 2010, MNRAS, 409, 421
- Geach, J. E., Smail, I., Best, P. N., et al. 2008, MNRAS, 388, 1473
- Giavalisco, M., Ferguson, H. C., Koekemoer, A. M., et al. 2004, ApJL, 600, L93
- Grazian, A., Fontana, A., de Santis, C., et al. 2006, A&A, 449, 951
- Grogin N. A., Kocevski, D. D., Faber, S. M., et al. 2011, ApJS, 197, 35
- Grützbauch, R., Conselice, C. J., Bauer, A. E., et al. 2011, MNRAS, 418, 938
- Grützbauch, R., Conselice, C. J., Bauer, A. E., et al. 2011, MNRAS, 418, 938
- Hathi, N. P., Malhotra, S., Rhoads, and J. E., 2008, ApJ, 673, 686
- Hathi, N. P., Ferreras, I., Pasquali, A., et al. 2009, ApJ, 690, 1866
- Herenz, E. C., Urrutia, T., Wisotzki, L., et al. 2017, A&A, 606, A12
- Horne K., 1986, PASP, 98, 609
- Inami, H., Bacon, R., Brinchmann, J., et al. 2017, A&A, 608, A2
- Kauffmann, G., White, S. D. M., Heckman, T. M., et al. 2004, MNRAS, 353, 713
- Kennicutt R. C., Jr, Roettiger K. A., Keel W. C., van der Hulst, J. M., Hummel E., 1987, AJ, 93, 1011
- Kennicutt, R. C., Jr. 1998, ARA&A, 36, 189
- Kobulnicky, H. A. & Zaritsky, D. 1999, ApJ, 511, 118
- Kocevski, D. D., Faber, S. M., Mozena, M., et al. 2012, ApJ, 744, 148
- Koekemoer, A.M., Faber, S.M., Ferguson, H.C., et al. 2011, ApJS, 197, 36
- Kriek, M., van Dokkum, P. G., Labbé, I., et al. 2009, ApJ, 700, 221
- Kriek, M., Shapley, A. E., Reddy, N. A., et al. 2015, ApJS, 218, 15
- Kurk, J., Cimatti, A., Daddi, E., et al. 2012, A&A, 549, 63

- Larson, R. L., Finkelstein, S. L., Pirzkal, N., et al. 2018, *ApJ*, 858, 94
- Le Fevre, O., Cassata, P., Cucciati, O., et al. 2013, *A&A*, 559, 14
- Le Fevre, O., Tasca, L. A. M., Cassata, P., et al. 2015, *A&A*, 576, A79
- Madau, P., Pozzetti, L., & Dickinson, M. 1998, *ApJ*, 498, 106
- Malhotra, S., Rhoads, J. E., Pirzkal, N. et al. 2005, *ApJ*, 626, 666
- McLure, R. J., Pentericci, L., Cimatti, A., et al. 2018, *MNRAS*, 479, 25
- Mo H. J., Jing Y. P., White S. D. M., 1996, *MNRAS*, 282, 1096
- Momcheva, I. G., Brammer, G. B., van Dokkum, P. G., et al. 2016, *ApJS*, 225, 27
- Morris, A. M., Kocevski, D. D., Trump, J. R., et al. 2015, *AJ*, 149, 178
- Muzzin, A., Wilson, G., Yee, H. K. C., et al., 2014, *ApJ*, 746, 188
- Muzzin, A., van der Burg, R. F. J., McGee, S. L., et al., 2012, *ApJ*, 796, 65
- Newville M., Stensitzki T., Allen D. B. and Ingargiola A. 2014 LMFIT: Non-Linear Least-Square Minimization and Curve-Fitting for Python zenodo, doi:10.5281/zenodo.11813
- Noeske, K. G., Faber, S. M., Weiner, B. J., et al., 2007, *ApJ*, 660, 47
- Oke, J. B., & Gunn, J. E. 1983, *ApJ*, 266, 713
- Ono, Y., Ouchi, M., Mobasher, B., et al. 2012, *ApJ*, 744, 83
- Pasquali, A., Pirzkal, N., Walsh, J. R., et al. 2003, *Astronomy, Cosmology and Fundamental Physics*, 471
- Pasquali, A., Ferreras, I., Panagia, N., et al. 2006, *ApJ*, 636, 115
- Pasquali, A., van den Bosch, F. C., Mo, H. J., Yang, X., and Somerville, R., 2009, *ApJ*, 394, 38
- Patel, S. G., Holden, B. P., Kelson, D. D., Illingworth, G. D., & Franx, M. 2009, *ApJL*, 705, L67
- Pentericci, L., McLure, R. J., Garilli, B., et al. 2018, *A&A*, 616, A174
- Pharo J., Malhotra, S., Rhoads, J. E., et al., 2018, *ApJ*, 856, 116
- Pirzkal, N., Xu, C., Malhotra, S., et al. 2004, *ApJS*, 154, 501
- Pirzkal, N., Burgasser, A. J., Malhotra, S., et al. 2009, *ApJ*, 695, 1591
- Pirzkal, N., Rothberg, B., Ly, C., et al. 2013, *ApJ*, 772, 48
- Pirzkal, N., Malhotra, S., Ryan, R. E., et al. 2017, *ApJ*, 846, 84
- Pirzkal, N., Rothberg, B., Ryan, R. E., et al. 2018, *ApJ*, 868, 61
- Planck Collaboration, Ade, P. A. R., Aghanim, N., et al. 2014, *A&A*, 571, A16
- Ramraj, R., Gilbank, D. G., Blyth, S.-L., Skelton, R. E., Glazebrook, K., Bower, R. G., & Balogh, M. L. 2017, *MNRAS*, 466, 3143
- Ravikumar, C. D., Puech, M.; Flores, H., et al. 2007, *A&A*, 465, 1099
- Reddy, N. A., Steidel, C. C., Erb, D. K., et al. 2006, *ApJ*, 653, 1004
- Rhoads, J. E., Malhotra, S., Dey, A., Jannuzi, B. T., Stern, D., & Spinrad, H. 2001, *ApJ*, 232, 196
- Rhoads, J. E., Panagia, N., Windhorst, R. A., et al., 2005, *ApJ*, 621, 582
- Rhoads, J. E., Malhotra, S., Pirzkal, N. et al. 2009, *ApJ*, 697, 942
- Rhoads, J. E., Malhotra, S., Stern, D., et al., 2013, *ApJ*, 773, 32
- Ryan, R. E. J., Hathi, N. P., Cohen, S. H., et al. 2007, *ApJ*, 668, 839
- Ryan, R., 2013, *HST Prop* 13266
- Santini, P., Ferguson, H. C., Fontana, A., et al. 2015, *ApJ*, 801, 97
- Scoville, N., Arnouts, S., Aussel, H., et al. 2013, *ApJS*, 206, 3
- Silverman, J. D., Mainieri, V., Salvato, M., et al. 2010, *ApJS*, 191, 124
- Skelton, R. E., Whitaker, K. E., Momcheva, I. G., et al. 2014, *ApJS*, 214, 24
- Sobral, D., Best, P. N., Smail, I., et al. 2011, *MNRAS*, 411, 675
- Sobral, D., Best, P. N., Matsuda, Y., et al. 2012, *MNRAS*, 420, 1926
- Song, M., Finkelstein, S. L., Gebhardt, K., et al. 2014, *ApJ*, 791, 3
- Soto, K. T., Lilly, S. J., Bacon, R., Richard, J., & Conseil, S. 2016, *MNRAS*, 458, 3210
- Spitler, L. R., Labb, I., Glazebrook, K., et al. 2012, *ApJ*, 748, L21
- Storey, P. J., & Zeppen, C. J. 2000, *MNRAS*, 312, 813
- Straughn, A. N., Meurer, G. R., Pirzkal, N., et al. 2008, *AJ*, 135, 1624
- Straughn, A. N., Pirzkal, N., Meurer, G. R., et al. 2009, *AJ*, 138, 1022

- Tilvi, V., Pirzkal, N., Malhotra, S. et al. 2016, ApJL, 827, 14
- Tran, K.-V. H., Papovich, C., Saintonge, A., et al. 2010, ApJL, 719, L126
- Treu, T., Schmidt, K. B., Brammer, G. B. et al. 2015, ApJ, 812, 114
- Trump, J. R., Konidaris, N. P., Barro, G., et al. 2013, ApJ, 763, 6
- Trump, J. R., Sun, M., Zeimann, G. R., et al. 2015, ApJ, 811, 26
- Vanzella, E., Cristiani, S., Dickinson, M., et al. 2008, A&A, 478, 83
- Vanzella, E., Giavalisco, M., Dickinson, M., et al. 2009, ApJ, 695, 1163
- Wirth, G. D., Willmer, C. N. A., Amico, P., et al. 2004, AJ, 127, 3121
- Wirth, G. D., Trump, J. R., Barro, G., et al. 2015, AJ, 150, 153
- Wuyts, S., Labbé, I., Förster S., et al. 2008, ApJ, 682, 985
- Wuyts, S., van Dokkum, P. G., Franx, M., et al. 2009, ApJ, 706, 885
- Xia, L., Malhotra, S., Rhoads, J. E., et al., 2011, AJ, 141, 64
- Xia, L., Malhotra, S., Rhoads, J., et al. 2012, AJ, 144, 28
- Xu C., Pirzkal N., Malhotra S. et al 2007 AJ 134 169
- Xue, Y. Q., Luo, B., Brandt, W. N., et al. 2011, ApJS, 195, 10
- Yang X., Mo H. J., van den Bosch F. C., Jing Y. P., 2005, MNRAS, 357, 608
- Yoshikawa, T., Akiyama, M., Kajisawa, M., et al. 2010, ApJ, 718, 112

APPENDIX
APPENDIX A: COMPLETE LINE FLUX CATALOG

Table 2.

Field	ID	RA (Deg)	Dec (Deg)	F105W (AB Mag)	Line	Flux (10^{-18} erg s $^{-1}$ cm $^{-2}$)	z_{line}	EW (Å)
GN1	1134	189.167313	62.306263	24.4	H α	17.1 ± 3.7	0.636	41 ± 8
GN1	1144	189.139786	62.305721	22.6	H α	66.3 ± 12.6	0.557	37 ± 6
GN1	1225	189.201447	62.304108	22.4	H α	116.5 ± 88.2	0.636	55 ± 40
GN1	1289	189.172318	62.302406	23.2	H α	59.2 ± 7.7	0.529	41 ± 5
GN1	1297	189.156693	62.302139	24.2	H α	42.5 ± 11.6	0.384	57 ± 15
GN1	1339	189.193359	62.30109	22.9	H α	92.7 ± 21.5	0.672	55 ± 12
GN1	1344	189.182663	62.301079	23.8	[OIII] $\lambda\lambda 4959, 5007$	52.3 ± 11.2	1.014	69 ± 13
GN1	1354	189.178833	62.300762	24.7	[OIII] $\lambda\lambda 4959, 5007$	22.6 ± 10.1	1.09	52 ± 22
GN1	1413	189.134064	62.299328	22.7	[OIII] $\lambda\lambda 4959, 5007$	121.3 ± 13.3	1.013	55 ± 6
GN1	1458	189.199326	62.29826	23.5	H α	32.5 ± 7.9	0.647	48 ± 12
GN1	1485	189.143372	62.297356	21.6	H α	91.3 ± 15.6	0.684	27 ± 4
GN1	1494	189.149567	62.297413	24.2	H α	28.3 ± 6.2	0.678	44 ± 9
GN1	1497	189.15683	62.296238	20.6	H α	369.6 ± 75.1	0.554	42 ± 8
GN1	1499	189.140961	62.297306	24.6	[OIII] $\lambda\lambda 4959, 5007$	47.4 ± 8.8	0.799	62 ± 11
GN1	1508	189.150726	62.297047	22.9	H α	75.1 ± 11.1	0.711	42 ± 6
GN1	1539	189.132751	62.295826	21.1	H α	122.8 ± 29.8	0.684	27 ± 6
GN1	1583	189.164795	62.295155	23.0	[OII] $\lambda 3727$	113.0 ± 19.5	2.049	86 ± 15
GN1	1589	189.153412	62.295105	25.4	[OIII] $\lambda\lambda 4959, 5007$	39.8 ± 8.6	0.964	59 ± 13
GN1	1610	189.15947	62.294628	23.2	H α	36.3 ± 10.4	0.604	40 ± 11
GN1	1640	189.186539	62.293983	23.6	H α	55.0 ± 9.0	0.456	49 ± 7
GN1	1647	189.184692	62.29356	21.1	H α	441.0 ± 97.9	0.451	61 ± 13
GN1	1681	189.161194	62.293125	26.0	[OIII] $\lambda\lambda 4959, 5007$	45.3 ± 7.8	1.022	67 ± 11
GN1	1715	189.149933	62.292282	24.2	H α	25.3 ± 7.5	0.68	38 ± 12
GN1	1734	189.139267	62.291878	23.5	[OIII] $\lambda\lambda 4959, 5007$	14.6 ± 5.4	1.284	19 ± 7
GN1	1747	189.1521	62.29171	23.7	[OIII] $\lambda\lambda 4959, 5007$	50.9 ± 9.8	1.218	59 ± 11
GN1	1750	189.173691	62.291481	21.8	H α	98.8 ± 18.8	0.486	34 ± 6
GN1	1756	189.151215	62.29155	24.2	[OII] $\lambda 3727$	41.1 ± 9.4	1.793	59 ± 13
GN1	1823	189.131577	62.289875	24.2	H α	37.1 ± 6.1	0.537	55 ± 9
GN1	1831	189.159225	62.289642	25.0	[OIII] $\lambda\lambda 4959, 5007$	87.2 ± 10.2	0.801	78 ± 9

Table 2 continued on next page

Table 2 (*continued*)

Field	ID	RA (Deg)	Dec (Deg)	F105W (AB Mag)	Line	Flux (10^{-18} erg s $^{-1}$ cm $^{-2}$)	z_{line}	EW (Å)
GN1	1841	189.203278	62.28941	24.9	[OIII] $\lambda\lambda 4959, 5007$	84.0 ± 9.4	0.955	104 ± 11
GN1	1957	189.180191	62.286591	25.1	[OIII] $\lambda\lambda 4959, 5007$	120.3 ± 10.8	0.795	68 ± 6
GN1	1973	189.145004	62.286209	24.4	[OII] $\lambda 3727$	34.9 ± 7.8	1.632	48 ± 10
GN1	2026	189.161438	62.285141	21.3	H α	379.0 ± 65.1	0.683	64 ± 10
GN1	2033	189.182953	62.284897	21.3	H α	186.4 ± 34.4	0.505	37 ± 6
GN1	2050	189.135483	62.283173	18.5	H α	54.4 ± 27.1	0.322	1 ± 0
GN1	2120	189.163193	62.28294	24.7	[OII] $\lambda 3727$	16.0 ± 5.1	1.687	38 ± 12
GN1	2132	189.128632	62.282539	23.1	[OIII] $\lambda\lambda 4959, 5007$	52.6 ± 10.9	0.94	52 ± 11
GN1	2135	189.162811	62.282536	23.6	[OIII] $\lambda\lambda 4959, 5007$	150.4 ± 12.3	1.014	75 ± 6
GN1	2327	189.142426	62.278187	22.3	H α	105.2 ± 20.7	0.502	44 ± 8
GN1	2371	189.175491	62.277306	24.3	[OIII] $\lambda\lambda 4959, 5007$	33.1 ± 12.0	0.949	60 ± 22
GN1	2394	189.164597	62.276897	25.8	[OIII] $\lambda\lambda 4959, 5007$	28.5 ± 10.4	1.243	125 ± 47
GN1	2412	189.199005	62.276527	24.8	[OIII] $\lambda\lambda 4959, 5007$	108.0 ± 12.9	0.779	76 ± 9
GN1	2449	189.181458	62.275795	23.3	[OII] $\lambda 3727$	35.8 ± 12.3	1.487	37 ± 13
GN1	2713	189.188126	62.270935	23.5	[OII] $\lambda 3727$	38.9 ± 8.7	1.445	53 ± 11
GN2	488	189.378052	62.325283	24.4	[OII] $\lambda 3727$	34.6 ± 9.0	2.008	65 ± 14
GN2	506	189.35556	62.323696	23.4	H α	38.0 ± 16.5	0.335	26 ± 10
GN2	507	189.395798	62.323574	21.5	H α	153.7 ± 29.4	0.635	37 ± 7
GN2	514	189.370529	62.323437	24.3	[OIII] $\lambda\lambda 4959, 5007$	64.3 ± 8.1	0.861	75 ± 9
GN2	554	189.397171	62.32164	20.7	[OIII] $\lambda\lambda 4959, 5007$	285.0 ± 33.6	0.835	32 ± 3
GN2	591	189.34729	62.31987	24.9	[OII] $\lambda 3727$	17.2 ± 11.1	1.995	61 ± 34
GN2	598	189.369843	62.319496	24.2	[OII] $\lambda 3727$	27.5 ± 7.1	1.599	55 ± 14
GN2	657	189.358841	62.3158	23.6	[OII] $\lambda 3727$	41.4 ± 8.7	1.595	49 ± 10
GN2	659	189.405548	62.315742	23.7	[OIII] $\lambda\lambda 4959, 5007$	39.4 ± 9.0	1.08	63 ± 13
GN2	682	189.390213	62.319218	23.2	[OII] $\lambda 3727$	66.9 ± 18.0	1.344	58 ± 15
GN2	717	189.414581	62.313183	22.4	H α	129.7 ± 23.3	0.338	46 ± 8
GN2	724	189.390701	62.312847	23.3	[OII] $\lambda 3727$	73.4 ± 10.9	2.005	51 ± 7
GN2	740	189.349564	62.311909	23.0	H α	32.6 ± 10.2	0.558	38 ± 12
GN2	745	189.382751	62.311504	22.8	[OIII] $\lambda\lambda 4959, 5007$	185.9 ± 20.2	1.084	98 ± 10
GN2	746	189.402069	62.311489	24.4	[OIII] $\lambda\lambda 4959, 5007$	68.4 ± 12.4	1.086	113 ± 174
GN2	756	189.369843	62.310909	22.3	H α	81.7 ± 12.5	0.519	37 ± 5
GN2	757	189.421219	62.310848	22.1	H α	76.5 ± 17.3	0.576	38 ± 8
GN2	759	189.401138	62.310909	24.2	[OII] $\lambda 3727$	32.8 ± 8.4	1.572	53 ± 13

Table 2 continued on next page

Table 2 (*continued*)

Field	ID	RA (Deg)	Dec (Deg)	F105W (AB Mag)	Line	Flux (10^{-18} erg s $^{-1}$ cm $^{-2}$)	z_{line}	EW (Å)
GN2	780	189.347214	62.310238	24.4	[OIII] $\lambda\lambda 4959, 5007$	58.7 ± 9.4	1.052	68 ± 10
GN2	782	189.387894	62.310043	24.5	[OIII] $\lambda\lambda 4959, 5007$	33.6 ± 7.2	0.982	70 ± 14
GN2	814	189.33992	62.308514	24.2	[OII] $\lambda 3727$	36.3 ± 5.6	1.973	72 ± 10
GN2	815	189.37941	62.308392	22.8	[OIII] $\lambda\lambda 4959, 5007$	109.3 ± 11.5	1.197	67 ± 7
GN2	836	189.391006	62.307247	21.9	H α	101.1 ± 19.3	0.562	38 ± 7
GN2	852	189.398239	62.306988	24.2	[OII] $\lambda 3727$	18.8 ± 4.8	2.051	42 ± 10
GN2	881	189.376816	62.305573	24.6	[OII] $\lambda 3727$	31.9 ± 6.5	1.926	53 ± 10
GN2	909	189.416992	62.304211	25.5	[OII] $\lambda 3727$	21.1 ± 6.4	1.781	85 ± 26
GN2	918	189.34906	62.303965	23.5	[OIII] $\lambda\lambda 4959, 5007$	306.6 ± 207.3	1.078	121 ± 93
GN2	938	189.419174	62.302856	22.4	[OIII] $\lambda\lambda 4959, 5007$	95.1 ± 14.1	1.027	47 ± 7
GN2	967	189.391983	62.301613	25.2	[OIII] $\lambda\lambda 4959, 5007$	41.7 ± 8.1	1.224	71 ± 13
GN2	969	189.367142	62.30154	25.4	[OIII] $\lambda\lambda 4959, 5007$	33.8 ± 6.7	1.146	75 ± 14
GN2	1049	189.385056	62.297539	24.2	[OII] $\lambda 3727$	46.9 ± 13.2	2.006	71 ± 17
GN2	1065	189.364334	62.29715	23.9	[OIII] $\lambda\lambda 4959, 5007$	77.1 ± 12.2	1.012	64 ± 11
GN2	1107	189.362579	62.295631	25.0	[OII] $\lambda 3727$	14.2 ± 8.4	2.051	40 ± 29
GN2	1114	189.387207	62.29525	23.3	[OIII] $\lambda\lambda 4959, 5007$	97.3 ± 12.1	0.773	54 ± 6
GN2	1145	189.355164	62.294254	24.1	[OIII] $\lambda\lambda 4959, 5007$	31.8 ± 9.9	0.942	33 ± 10
GN2	1160	189.356705	62.293705	23.4	[OII] $\lambda 3727$	36.3 ± 8.9	1.526	49 ± 11
GN2	1186	189.385986	62.292267	23.9	[OII] $\lambda 3727$	31.3 ± 6.1	1.774	61 ± 12
GN2	1227	189.376297	62.290405	24.0	[OII] $\lambda 3727$	36.2 ± 10.6	1.682	73 ± 21
GN2	1240	189.393906	62.289795	20.1	H α	194.1 ± 18.9	0.639	18 ± 1
GN2	1265	189.364151	62.289097	24.6	H α	27.4 ± 4.7	0.633	50 ± 8
GN2	1319	189.387177	62.287018	22.7	H α	90.1 ± 18.5	0.632	63 ± 13
GN2	3114	189.376511	62.325085	25.5	[OIII] $\lambda\lambda 4959, 5007$	31.8 ± 11.6	0.839	135 ± 91
GN2	3574	189.389481	62.315483	27.1	[OIII] $\lambda\lambda 4959, 5007$	54.2 ± 10.1	0.863	57 ± 11
GN2	4969	189.363007	62.287544	25.9	[OII] $\lambda 3727$	47.7 ± 15.3	1.363	423 ± 171
GS1	724	53.172264	-27.760622	22.6	[OII] $\lambda 3727$	68.7 ± 19.8	1.552	39 ± 11
GS1	950	53.161499	-27.76762	23.4	H α	38.1 ± 10.5	0.679	34 ± 7
GS1	970	53.160183	-27.769306	24.1	[OIII] $\lambda\lambda 4959, 5007$	69.0 ± 11.2	1.044	88 ± 14
GS1	1013	53.169926	-27.771027	20.0	H α	156.7 ± 25.6	0.618	14 ± 2
GS1	1016	53.172104	-27.770382	23.6	H α	18.2 ± 3.8	0.631	34 ± 7
GS1	1056	53.162453	-27.770908	24.3	[OIII] $\lambda\lambda 4959, 5007$	35.6 ± 4.2	1.036	88 ± 10
GS1	1103	53.174	-27.772057	20.7	H α	198.7 ± 27.6	0.335	23 ± 3

Table 2 continued on next page

Table 2 (*continued*)

Field	ID	RA (Deg)	Dec (Deg)	F105W (AB Mag)	Line	Flux (10^{-18} erg s $^{-1}$ cm $^{-2}$)	z_{line}	EW (Å)
GS1	1132	53.184479	-27.772245	24.6	[OIII] $\lambda\lambda 4959, 5007$	31.9 ± 7.6	0.835	50 ± 12
GS1	1151	53.152878	-27.772497	24.6	[OII] $\lambda 3727$	20.0 ± 7.4	1.851	48 ± 18
GS1	1171	53.151215	-27.772837	23.8	H α	49.4 ± 8.2	0.607	47 ± 7
GS1	1239	53.191463	-27.77389	23.5	H α	32.7 ± 9.7	0.419	36 ± 10
GS1	1295	53.162361	-27.775063	20.6	H α	352.9 ± 61.4	0.419	39 ± 6
GS1	1296	53.159355	-27.775028	23.1	[OIII] $\lambda\lambda 4959, 5007$	41.9 ± 16.9	1.22	45 ± 18
GS1	1299	53.160801	-27.775373	21.2	H α	110.2 ± 27.4	0.623	27 ± 6
GS1	1359	53.185909	-27.775608	22.9	[OII] $\lambda 3727$	78.3 ± 20.6	1.425	60 ± 15
GS1	1392	53.181046	-27.776175	22.1	H α	102.0 ± 22.9	0.668	40 ± 8
GS1	1467	53.151047	-27.777309	24.1	[OIII] $\lambda\lambda 4959, 5007$	32.2 ± 7.6	0.733	55 ± 12
GS1	1467	53.151047	-27.777309	24.1	H α	28.4 ± 10.6	0.733	52 ± 21
GS1	1476	53.147438	-27.777596	23.6	[OII] $\lambda 3727$	30.5 ± 8.5	1.851	48 ± 13
GS1	1477	53.158291	-27.777449	24.5	[OII] $\lambda 3727$	26.7 ± 6.6	1.557	41 ± 10
GS1	1481	53.146614	-27.777489	25.0	[OIII] $\lambda\lambda 4959, 5007$	20.5 ± 12.3	1.091	47 ± 24
GS1	1500	53.152336	-27.777948	24.3	[OII] $\lambda 3727$	30.0 ± 7.1	1.42	50 ± 12
GS1	1552	53.157204	-27.778522	23.8	[OII] $\lambda 3727$	24.2 ± 22.0	1.31	34 ± 29
GS1	1689	53.162483	-27.780346	25.1	H α	37.9 ± 8.7	0.722	52 ± 12
GS1	1689	53.162483	-27.780346	25.1	[OIII] $\lambda\lambda 4959, 5007$	63.6 ± 12.3	0.722	65 ± 12
GS1	1710	53.172619	-27.78096	21.4	H α	111.4 ± 24.5	0.62	32 ± 7
GS1	1711	53.196999	-27.780598	23.9	[OIII] $\lambda\lambda 4959, 5007$	36.0 ± 7.2	0.739	46 ± 8
GS1	1728	53.176331	-27.780861	25.0	[OIII] $\lambda\lambda 4959, 5007$	42.0 ± 10.1	1.016	60 ± 14
GS1	1803	53.170067	-27.782066	26.7	[OII] $\lambda 3727$	55.1 ± 8.8	1.344	81 ± 12
GS1	1829	53.150764	-27.78256	24.2	[OII] $\lambda 3727$	74.6 ± 9.7	1.343	92 ± 11
GS1	1851	53.152782	-27.782698	24.4	[OIII] $\lambda\lambda 4959, 5007$	101.1 ± 10.5	0.768	72 ± 7
GS1	1864	53.175331	-27.782722	26.0	[OIII] $\lambda\lambda 4959, 5007$	36.9 ± 19.6	0.843	152 ± 81
GS1	1867	53.15184	-27.782864	23.2	H α	66.3 ± 13.6	0.406	40 ± 8
GS1	1900	53.184574	-27.783323	24.4	[OIII] $\lambda\lambda 4959, 5007$	98.8 ± 15.8	1.137	76 ± 12
GS1	1946	53.192593	-27.783791	24.7	[OIII] $\lambda\lambda 4959, 5007$	65.8 ± 11.7	0.869	105 ± 18
GS1	2023	53.151863	-27.784752	25.6	[OIII] $\lambda\lambda 4959, 5007$	33.0 ± 9.6	1.217	86 ± 25
GS1	2029	53.157948	-27.784767	28.1	[OIII] $\lambda\lambda 4959, 5007$	22.4 ± 9.5	0.719	34 ± 14
GS1	2029	53.157948	-27.784767	28.1	H α	15.1 ± 7.7	0.719	23 ± 11
GS1	2039	53.166565	-27.784861	27.6	[OII] $\lambda 3727$	17.2 ± 9.0	1.304	109 ± 57
GS1	2077	53.161686	-27.785322	27.5	H α	29.7 ± 9.4	0.337	87 ± 27

Table 2 continued on next page

Table 2 (*continued*)

Field	ID	RA (Deg)	Dec (Deg)	F105W (AB Mag)	Line	Flux (10^{-18} erg s $^{-1}$ cm $^{-2}$)	z_{line}	EW (Å)
GS1	2138	53.160477	-27.786299	24.3	[OIII] $\lambda\lambda 4959, 5007$	35.3 ± 7.5	0.983	57 ± 11
GS1	2168	53.163471	-27.786636	25.1	H α	17.6 ± 5.1	0.469	47 ± 14
GS1	2187	53.177753	-27.786966	24.4	[OIII] $\lambda\lambda 4959, 5007$	38.3 ± 9.9	0.95	75 ± 20
GS1	2221	53.164097	-27.787298	23.8	[OIII] $\lambda\lambda 4959, 5007$	190.9 ± 12.2	1.098	64 ± 4
GS1	2291	53.149296	-27.788527	23.0	[OII] $\lambda 3727$	65.3 ± 15.1	1.916	52 ± 12
GS1	2338	53.15736	-27.789219	25.1	[OIII] $\lambda\lambda 4959, 5007$	35.5 ± 9.4	0.999	85 ± 24
GS1	2363	53.168015	-27.789671	22.8	H α	79.4 ± 16.8	0.621	55 ± 11
GS1	2375	53.176495	-27.789705	24.9	H α	26.1 ± 8.1	0.427	42 ± 13
GS1	2378	53.18795	-27.790001	20.3	H α	749.5 ± 279.4	0.438	47 ± 17
GS1	2385	53.184811	-27.789934	23.1	[OIII] $\lambda\lambda 4959, 5007$	43.2 ± 10.7	0.956	45 ± 11
GS1	2417	53.160419	-27.790369	23.5	[OII] $\lambda 3727$	41.5 ± 8.7	1.617	44 ± 9
GS1	2495	53.184132	-27.791531	23.1	[OIII] $\lambda\lambda 4959, 5007$	7.3 ± 10.7	1.214	8 ± 11
GS1	2517	53.161613	-27.792299	20.6	H α	1404.0 ± 251.4	0.462	65 ± 11
GS1	2560	53.184158	-27.792637	21.4	[OIII] $\lambda\lambda 4959, 5007$	162.6 ± 18.2	0.739	107 ± 12
GS1	2560	53.184158	-27.792637	21.4	H α	203.3 ± 53.7	0.739	84 ± 23
GS1	2570	53.164124	-27.792654	27.0	[OII] $\lambda 3727$	16.5 ± 31.8	1.301	36 ± 64
GS1	2654	53.182205	-27.793993	24.8	H α	20.8 ± 11.7	1.28	60 ± 33
GS1	2669	53.156631	-27.794302	24.3	[OIII] $\lambda\lambda 4959, 5007$	41.5 ± 10.3	1.098	61 ± 14
GS1	2696	53.155861	-27.794901	22.9	[OIII] $\lambda\lambda 4959, 5007$	104.1 ± 31.9	1.1	74 ± 22
GS1	2720	53.15675	-27.79558	21.8	[OIII] $\lambda\lambda 4959, 5007$	90.5 ± 18.7	1.099	42 ± 11
GS1	2732	53.161331	-27.795797	23.6	[OII] $\lambda 3727$	50.7 ± 13.2	1.495	50 ± 13
GS1	2783	53.188084	-27.795742	24.0	H α	116.4 ± 8.9	0.536	47 ± 3
GS1	2872	53.16687	-27.797707	23.7	[OIII] $\lambda\lambda 4959, 5007$	70.2 ± 14.2	0.99	75 ± 15
GS1	2942	53.161121	-27.798801	25.5	[OIII] $\lambda\lambda 4959, 5007$	27.9 ± 13.5	1.228	82 ± 34
GS1	4184	53.179535	-27.766174	25.1	H α	15.7 ± 5.8	0.67	35 ± 12
GS1	4198	53.178375	-27.76824	20.2	H α	341.1 ± 49.8	0.674	32 ± 4
GS1	4258	53.152287	-27.770088	23.7	[OII] $\lambda 3727$	45.4 ± 14.5	1.854	50 ± 16
GS1	4284	53.184544	-27.768221	25.2	[OII] $\lambda 3727$	7.2 ± 4.3	1.842	14 ± 8
GS1	6865	53.190331	-27.774298	26.8	[OIII] $\lambda\lambda 4959, 5007$	18.2 ± 12.1	0.883	54 ± 35
GS1	8178	53.187664	-27.783779	27.0	[OIII] $\lambda\lambda 4959, 5007$	22.0 ± 7.6	0.737	110 ± 38
GS2	575	53.28241	-27.843513	24.0	[OIII] $\lambda\lambda 4959, 5007$	87.8 ± 16.6	0.739	73 ± 14
GS2	575	53.28241	-27.843513	24.0	H α	68.5 ± 16.9	0.739	61 ± 15
GS2	577	53.273159	-27.844625	25.9	[OIII] $\lambda\lambda 4959, 5007$	24.2 ± 9.7	1.231	66 ± 25

Table 2 continued on next page

Table 2 (*continued*)

Field	ID	RA (Deg)	Dec (Deg)	F105W (AB Mag)	Line	Flux (10^{-18} erg s $^{-1}$ cm $^{-2}$)	z_{line}	EW (Å)
GS2	596	53.274158	-27.84565	23.2	[OII] λ 3727	34.8 ± 7.4	1.686	36 ± 7
GS2	599	53.279076	-27.845737	23.1	[OIII] $\lambda\lambda$ 4959, 5007	318.9 ± 40.1	0.737	71 ± 8
GS2	599	53.279076	-27.845737	23.1	H α	228.1 ± 59.8	0.737	55 ± 14
GS2	620	53.272892	-27.847765	22.2	H α	81.0 ± 9.1	0.711	35 ± 3
GS2	709	53.288483	-27.851877	24.0	H α	22.4 ± 5.3	0.687	46 ± 11
GS2	782	53.281536	-27.854385	23.7	[OIII] $\lambda\lambda$ 4959, 5007	81.2 ± 10.8	0.834	56 ± 7
GS2	846	53.264668	-27.855431	24.6	[OII] λ 3727	26.7 ± 9.7	1.76	56 ± 20
GS2	868	53.275829	-27.855747	24.7	H α	33.4 ± 9.6	0.737	82 ± 23
GS2	871	53.266712	-27.856167	20.5	H α	559.4 ± 184.3	0.529	49 ± 16
GS2	887	53.291748	-27.856255	24.2	[OII] λ 3727	28.5 ± 11.2	1.815	56 ± 21
GS2	951	53.264828	-27.857828	24.3	[OII] λ 3727	66.2 ± 17.7	1.303	68 ± 17
GS2	951	53.264828	-27.857828	24.3	[OIII] $\lambda\lambda$ 4959, 5007	235.2 ± 20.1	1.291	107 ± 9
GS2	1038	53.285847	-27.85964	20.6	[OIII] $\lambda\lambda$ 4959, 5007	238.1 ± 97.6	0.725	33 ± 13
GS2	1038	53.285847	-27.85964	20.6	H α	754.1 ± 49.5	0.725	66 ± 4
GS2	1054	53.2869	-27.859509	22.8	[OII] λ 3727	56.6 ± 19.4	1.68	37 ± 12
GS2	1131	53.26556	-27.861135	23.6	[OIII] $\lambda\lambda$ 4959, 5007	37.9 ± 14.6	0.885	44 ± 14
GS2	1215	53.266247	-27.862015	23.9	[OII] λ 3727	21.3 ± 8.4	1.905	37 ± 14
GS2	1240	53.293732	-27.862436	inf	[OII] λ 3727	14.8 ± 3.2	1.901	49 ± 11
GS2	1270	53.275627	-27.863014	24.4	[OII] λ 3727	29.4 ± 7.8	2.012	72 ± 19
GS2	1280	53.283585	-27.864466	22.9	H α	74.4 ± 12.2	0.476	43 ± 6
GS2	1392	53.28775	-27.865278	24.3	H α	22.2 ± 5.2	0.612	44 ± 10
GS2	1483	53.272259	-27.867044	24.7	[OIII] $\lambda\lambda$ 4959, 5007	61.9 ± 8.5	0.979	73 ± 10
GS2	1552	53.266247	-27.868002	22.9	[OII] λ 3727	81.0 ± 21.8	1.761	50 ± 13
GS2	1593	53.272778	-27.868891	21.6	H α	135.9 ± 37.2	0.693	39 ± 10
GS2	1607	53.265091	-27.86924	21.7	H α	126.0 ± 32.7	0.524	46 ± 12
GS2	1630	53.264194	-27.869268	23.3	[OII] λ 3727	53.7 ± 18.7	1.817	51 ± 18
GS2	1653	53.273643	-27.870647	18.4	H α	515.4 ± 85.3	0.524	12 ± 2
GS2	1666	53.268139	-27.869875	24.2	[OIII] $\lambda\lambda$ 4959, 5007	97.4 ± 12.3	0.737	80 ± 10
GS2	1666	53.268139	-27.869875	24.2	H α	52.5 ± 10.7	0.737	53 ± 10
GS2	1772	53.28323	-27.872059	25.8	[OIII] $\lambda\lambda$ 4959, 5007	53.4 ± 9.5	1.176	73 ± 12
GS2	1836	53.2654	-27.873278	22.8	[OII] λ 3727	105.2 ± 22.1	1.988	57 ± 12
GS2	1845	53.276325	-27.873322	26.1	[OIII] $\lambda\lambda$ 4959, 5007	18082.0 ± 2131.0	1.044	51 ± 6
GS2	3186	53.291828	-27.845343	inf	H α	1500.3 ± 231.8	0.523	63 ± 9

Table 2 continued on next page

Table 2 (*continued*)

Field	ID	RA (Deg)	Dec (Deg)	F105W (AB Mag)	Line	Flux (10^{-18} erg s $^{-1}$ cm $^{-2}$)	z_{line}	EW (Å)
GS2	3259	53.276016	-27.847622	24.4	[OIII] $\lambda\lambda 4959, 5007$	339.3 ± 25.4	1.262	99 ± 10
GS2	3277	53.277046	-27.848417	24.6	[OII] $\lambda 3727$	21.0 ± 4.0	1.907	38 ± 7
GS2	3295	53.258167	-27.849049	23.4	[OII] $\lambda 3727$	96.4 ± 23.2	1.9	65 ± 15
GS2	3314	53.285191	-27.850237	24.3	[OII] $\lambda 3727$	27.5 ± 8.5	1.717	63 ± 19
GS2	3347	53.266071	-27.852331	22.0	H α	120.6 ± 26.7	0.548	50 ± 11
GS2	3418	53.253826	-27.856579	27.0	[OIII] $\lambda\lambda 4959, 5007$	39.6 ± 12.4	0.909	92 ± 28
GS2	3419	53.254498	-27.856409	24.3	H α	26.7 ± 5.4	0.521	42 ± 8